Title: Coordinate transcriptional and post-transcriptional repression of pro-differentiation genes maintains intestinal stem cell identity

Authors: Kasun Buddika[1], Yi-Ting Huang[1], Ishara S. Ariyapala[1], Alex Butrum-Griffith[*1], Sam A. Norrell[*1], Alex M. O'Connor[*1], Viraj K. Patel[*1], Samuel A. Rector[*1], Mark Slovan[*1], Mallory Sokolowski[*1], Yasuko Kato[2], Akira Nakamura[3], Nicholas S. Sokol[1]

Affiliation: [1]Department of Biology, Indiana University, Bloomington, IN 47405, USA, [2]Department of Applied Biology, Kyoto Institute of Technology, Matsugasaki, Sakyo-ku, Kyoto, 606-8585, Japan, [3] Department of Germline Development, Institute of Molecular Embryology and Genetics, Kumamoto University, 2-2-1 Honjo, Kumamoto 860-0811, Japan

*** equal contribution**

Correspondence: nsokol@indiana.edu (email)
812-856-6812 (phone)

Running Title: The structure and function of P-bodies in intestinal stem cells

29 **Highlights**

30 - Drosophila intestinal progenitor cells contain constitutive and ultrastructurally
31 organized P-bodies.
32 - A P-body regulator *Patr-1* is required for intestinal progenitor cell maintenance.
33 - Enterocyte (EC) genes such as *nubbin* are weakly transcribed but not translated
34 in intestinal progenitors.
35 - P-bodies repress EC gene translation to promote stem cell maintenance.

36 **Graphical abstract**

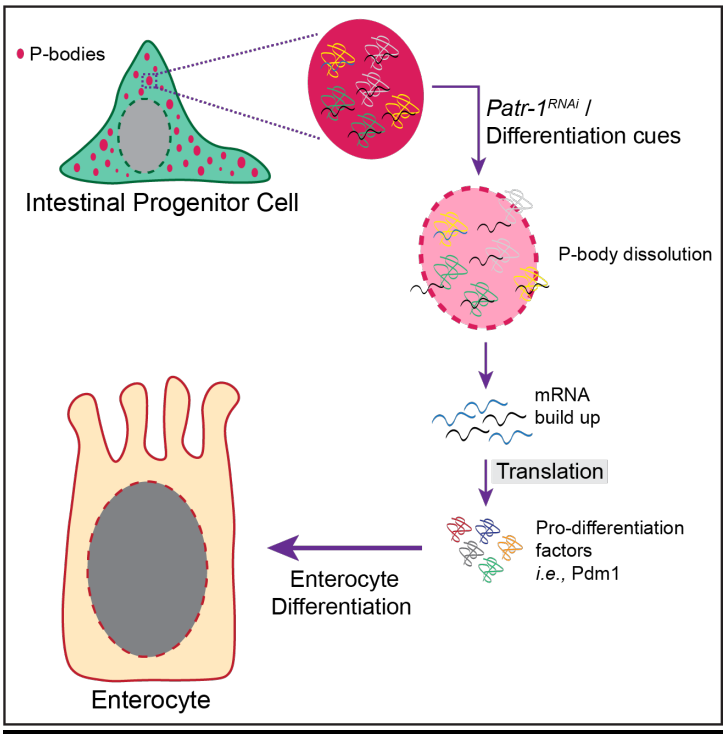

37

Summary

The role of Processing bodies (P-bodies), key sites of post-transcriptional control, in adult stem cells remains poorly understood. Here, we report that adult Drosophila intestinal stem cells, but not surrounding differentiated cells such as absorptive Enterocytes (ECs), harbor P-bodies that contain *Drosophila* orthologs of mammalian P-body components DDX6, EDC3, EDC4 and LSM14A/B. A targeted RNAi screen in intestinal progenitor cells identified 39 previously known and 64 novel P-body regulators, including *Patr-1*, a gene necessary for P-body assembly. Loss of *Patr-1*-dependent P-bodies leads to a loss of stem cells that is associated with inappropriate translation and expression of EC-fate gene *nubbin*. Transcriptomic analysis of progenitor cells identifies a cadre of such weakly transcribed pro-differentiation transcripts that are elevated after P-body loss. Altogether, this study identifies a coordinated P-body dependent, translational and transcriptional repression program that maintains a defined set of *in vivo* stem cells in a state primed for differentiation.

52 ## Introduction

53 In eukaryotic cells, translationally inactive messenger RNAs (mRNAs) can
54 assemble to form a distinct population of cytoplasmic messenger ribonucleoprotein
55 (mRNP) particles known as Processing bodies (P-bodies) (Anderson and Kedersha,
56 2006; Decker and Parker, 2012; Kedersha et al., 2005). Like stress granules, P-bodies
57 lack a limiting membrane and are visible via conventional microscopic techniques
58 (Anderson and Kedersha, 2006), are enhanced or induced by blocking translation
59 initiation (Buchan and Parker, 2009; Chan et al., 2018; Franks and Lykke-Andersen,
60 2008; Kedersha et al., 2000; Teixeira et al., 2005), are disassembled when treated with
61 cycloheximide, a chemical that traps mRNAs on ribosomes (Anderson and Kedersha,
62 2009; Buchan and Parker, 2009; Kedersha et al., 2000; Mugler et al., 2016; Teixeira et
63 al., 2005), and are conserved from yeast to humans (Martínez et al., 2013; Protter and
64 Parker, 2016). Unlike stress granules, however, P-bodies are constitutive and contain
65 proteins involved in mRNA decay (Anderson and Kedersha, 2006, 2009; Buchan and
66 Parker, 2009; Decker and Parker, 2012; Eulalio et al., 2007a; Luo et al., 2018; Parker
67 and Sheth, 2007; Sheth and Parker, 2003; Youn et al., 2019). While recent studies have
68 identified stress granules in stem cells of adult tissues (Buddika et al., 2020a), whether
69 P-bodies are also present in adult stem cells and, if so, what biological processes they
70 might control is not well understood.

71 Recent biochemical profiling experiments in human HEK293 cells identified
72 different classes of P-body resident proteins that include translation repression and
73 mRNA decay factors (4E-T, LSM14A, LSM14B and IGF2BP2), microRNA pathway
74 components (AGO1, AGO2 and MOV10), decapping complex proteins (DCP1A,
75 DCP1B, DCP2 and EDC4) and nonsense-mediated mRNA decay (NMD) factors (UPF1)
76 (Hubstenberger et al., 2017). Similar studies have also identified 6,168 transcripts to be
77 significantly enriched in P-bodies and another 7,588 transcripts to be significantly
78 depleted (Hubstenberger et al., 2017). This clear bifurcation of mRNAs indicates that
79 the P-body transcriptome is large but specific (Hubstenberger et al., 2017; Standart and
80 Weil, 2018). While its protein composition suggests that the primary function of P-bodies
81 is mRNA degradation (Anderson and Kedersha, 2006; Decker and Parker, 2012),
82 recent studies have found that mRNAs localized to P-bodies can return to the cytoplasm

83 to re-enter translation (Bhattacharyya et al., 2006; Brengues et al., 2005) and that P-
84 bodies can be disrupted without affecting mRNA decay (Eulalio et al., 2007a; Stoecklin
85 et al., 2006). Therefore, current models propose that P-bodies coordinate the storage of
86 mRNA regulons leading to stoichiometric protein production (Standart and Weil, 2018).
87 However, genetically tractable *in vivo* P-body models are necessary to better
88 understand the exact role of P-bodies in eukaryotic tissues including the identification
89 and tracking of P-body regulated mRNAs *in vivo*. Developing such tissue-based models
90 will also provide insights into the structural organization of P-bodies. While electron
91 micrographs of P-bodies in HeLa cells have identified densely populated structures
92 within P-bodies (Souquere et al., 2009), the integration of super-resolution based
93 characterizations are required to elucidate whether P-body resident components are
94 structurally organized (Youn et al., 2019).
95 Although some post-transcriptional processes such as alternative splicing,
96 polyadenylation, and RNA modifications have been extensively studied in pluripotent
97 stem cells (Chen and Hu, 2017), the roles of these and other RNA processes, such as
98 RNA decay, storage, and translational control, in the potency of adult somatic stem cells
99 remain poorly understood. For example, while recent work indicated that post-
100 transcriptional regulation of mRNAs via P-bodies play vital roles in adult stem cell
101 proliferation and differentiation, it is complex and dynamic: functional analysis of the P-
102 body protein DDX6 found that it promotes differentiation in some *in vitro* derived stem
103 cell lineages and represses it in others (Di Stefano et al., 2019). Thus, tissue-based
104 stem cell models will be critical for probing P-body function in an *in vivo* context. The
105 intestinal epithelium of adult *Drosophila* offers such a model to study post-transcriptional
106 gene regulatory mechanisms (Buddika et al., 2020a; Chen et al., 2015; Luhur et al.,
107 2017). This actively regenerating tissue hosts a population of progenitor cells, which is
108 composed of two main cell types: mitotic intestinal stem cells (ISCs) and their transient
109 and non-mitotic daughters, enteroblasts (EBs) (Micchelli and Perrimon, 2006; Ohlstein
110 and Spradling, 2006). In this study we used the Drosophila midgut as a tissue-based
111 stem cell model to delineate the biological roles of P-bodies *in vivo*.

112 ## Results

113

114 **P-body components are enriched in intestinal progenitor cells**

115 To test whether intestinal progenitor cells contained P-bodies, we stained
116 intestines dissected from 7-day old, adult female *Drosophila* with a series of four
117 antibodies. These detected the Drosophila orthologs of known P-body proteins in other
118 systems: EDC3, GE-1 (known in metazoans as EDC4), Me31B (known in metazoans as
119 DDX6), and TRAL (known in metazoans as LSM14A) (Anderson and Kedersha, 2006;
120 Ayache et al., 2015; Eulalio et al., 2007a; Hubstenberger et al., 2017). Using previously
121 verified antibodies for GE-1 and Me31B (Barbee et al., 2006; Fan et al., 2011;
122 Nakamura A, Amikura R, Hanyu K, 2001) as well as new, validated antibodies for TRAL
123 and EDC3 (**Fig. S1A-B**), we found that all these antibodies displayed elevated signal in
124 intestinal progenitors (**Fig. 1A-D**), which were labeled by horseradish peroxidase (HRP)
125 (Miller et al., 2020; O'Brien et al., 2011). Limited to the cytoplasm, confocal microscopy
126 detected these proteins in clearly separated cytoplasmic granules that were similar in
127 level and organization in both ISCs and *3Xgbe-smGFP::V5::nls* positive EBs (**Fig. 1A'-**
128 **D'**). TRAL and Me31B staining perfectly overlapped, indicating colocalization (**Fig. 1E-**
129 **E'**). The relative absence of staining in neighboring polyploid ECs also indicated that
130 these proteins were downregulated during EC differentiation (see **Fig. 1A-E**). To assess
131 whether such downregulation occurred during EE differentiation as well, we co-stained
132 intestines for Prospero (PROS), an EE-marker (Micchelli and Perrimon, 2006), and
133 either TRAL or Me31B. While the majority of PROS+ cells showed very low to no
134 detectable TRAL or Me31B, ~20% displayed levels that were comparable to progenitor
135 cells (**Fig. S1C-D**). These data indicated the presence of a population of cytoplasmic
136 granules containing colocalized P-body components in progenitor cells that were
137 cleared during EC and EE differentiation.

138

139 **Intestinal P-bodies are ultrastructurally organized**

140 Because the structural organization of P-bodies is not well understood (Youn et
141 al., 2019), we used this system to assess the ultrastructural organization of intestinal P-
142 body protein complexes. We stained dissected intestines with either Me31B, TRAL or

143 EDC3, imaged the cytoplasmic distribution of these proteins using structured
144 illumination super-resolution microscopy (SIM), and then used the FIJI package of
145 ImageJ to generate intensity maps of each protein. These maps revealed that the
146 distribution of Me31B, TRAL, and EDC3 was not uniform within a granule (**Fig. 1F, H,**
147 **J**). We noted that the pixel density was different along the length of a granule and more
148 central domains within the granule contained greater protein accumulation than the rest
149 of the granule (**Fig. 1G, I, K**). Given that this non-uniform protein organization within
150 mature P-bodies is very similar to the core-shell organization of a stress granule, we
151 propose that P-bodies share the same structural organization. Although significantly
152 smaller, P-bodies are likely to have multiple cores similar to stress granules. Taken
153 together, these data identified the existence of a structurally organized population of
154 steady-state P-bodies in intestinal progenitors of adult *Drosophila*.
155
156 **P-bodies and stress granules are distinct mRNPs in progenitor cells**
157 The above analysis suggested that P-body complexes were distinct from
158 intestinal progenitor stress granules (IPSGs) because P-bodies were present under
159 standard conditions while IPSG complexes only formed after intestines were exposed to
160 acute stress (Buddika et al., 2020a). We therefore compared the subcellular locations
161 and sizes of P-body proteins (TRAL/Me31b) with IPSG proteins (Fragile Mental
162 Retardation Protein [FMRP]/Rasputin[RIN]) in both unstressed and stressed conditions
163 using SIM. For these experiments, unstressed samples were prepared by incubating
164 dissected intestines *ex-vivo* in Krebs Ringer Bicarbonate Buffer (KRB) for 60 minutes;
165 stressed intestines were treated with 1mM rapamycin in KRB for the same length of
166 time. P-body proteins perfectly colocalized with each other under unstressed conditions
167 but only partially colocalized with IPSG proteins under these same conditions (**Fig. S1E-**
168 **J**). However, after stress, P-body and IPSG proteins perfectly localized (**Fig. S1K-P**). To
169 investigate the sizes of these complexes, we measured the sizes of TRAL and FMRP
170 punctae. Under unstressed conditions, TRAL punctae (0.047 μm^2; n=804 puncta in 14
171 cells) were bigger than FMRP punctae (0.026 μm^2; n=629 puncta in 8 cells] (**Fig. S1Q-**
172 **R, U**). Stress treatment caused TRAL punctae (0.097 μm^2; n=657 puncta in 25 cells)
173 and FMRP punctae (0.098 μm^2; n=1215 puncta in 42 cells) to grow to the same size

174 (**Fig. S1S-U**). From this analysis, we concluded that P-body proteins localized to
175 persistent mRNP complexes that, unlike IPSGs, were present in unstressed cells, and
176 that stress led to the enlargement of these mRNPs into IPSGs.
177
178 **Identification of genetic modifiers of progenitor P-bodies using a targeted screen**
179 To characterize the genetic framework governing P-body formation in progenitor
180 cells, we performed a targeted RNAi screen to identify genes that altered P-body
181 morphology. We focused on genes implicated in RNA-related processes, and generated
182 a list of 600 candidate genes by using the GO term analysis function on Flybase. We
183 selected the 485 genes with Bloomington *Drosophila* Stock Center RNAi strains to
184 conduct a primary screen, and used TRAL as the P-body marker to score for P-body
185 morphology (**Table S1**). We screened a total of 735 RNAi strains that targeted these
186 485 genes: 186 genes were targeted using two or more RNAi strains, and the
187 remainder were targeted by just one RNAi line. Individual RNAi strains were crossed to
188 a conditional version of the progenitor cell driver *esg-GAL4* (*esgTS*) (Micchelli and
189 Perrimon, 2006), induced at the adult stage, and dissected seven days later. From this
190 analysis, 103 genes that affected TRAL pattern or level were identified and grouped into
191 five phenotypic classes: [1] large TRAL puncta ("Big"), [2] small TRAL puncta ("Small"),
192 [3] dispersed TRAL puncta ("Diffuse"), [4] both dispersed and large TRAL puncta
193 ("Diffuse + Big"), and [5] no TRAL staining ("No TRAL") (**Fig. 2A-B**). To assess the
194 specificity of these effects on P-body morphology, a representative set of 25 positives --
195 13 "big" genes, 3 "small" genes, 4 "diffuse" genes, 3 "diffuse + big" genes, and 2 "no
196 TRAL" genes -- were also co-stained with IPSG-makers FMRP and ROX8 (**Fig. S2A-F,**
197 **Table S1**). While most had no discernable effect, two genes, *fne* and CG13928, altered
198 the expression profile of these IPSG proteins and led to "big" or "diffuse and big"
199 FMRP/ROX8 foci, respectively (**Table S1**, **Fig. S2E**). As expected, many of the positive
200 genes encode proteins that were implicated in mRNA metabolic processes (54 genes)
201 and were known components of ribonucleoprotein complexes (42 genes) (**Fig. S2G-H**).
202 For example, the targeting of genes encoding P-body resident proteins EDC3 or PCM,
203 the *Drosophila* homolog of mammalian 5'-3' exonuclease XRN1, led to bigger TRAL
204 granules. While 39 (38%) of the identified genes were orthologs of proteins known to

205 affect P-bodies in human cells (**Table S1**) (Youn et al., 2019), we also identified 64
206 (62%) genes that were not previously implicated in P-body organization or assembly.
207 Unexpectedly, regulators of nuclear processes such as RNA splicing (35 genes) and
208 nuclear export (9 genes) as well as components of nuclear assemblies such as the
209 exon-exon junction complex (6 genes) also impacted the morphology of cytoplasmic
210 TRAL granules (**Fig. S2G-H**, **Table S1**). We also noted that knockdown of 24% of the
211 positive genes (23/103 genes), caused loss of progenitor cells. These results therefore
212 raise the possibility that P-bodies are physiologically linked to the stemness of this
213 progenitor cell population.
214
215 **PATR-1 is a P-body resident protein that is necessary for their formation**
216 To investigate the function of P-bodies in progenitor cells in more detail, we
217 focused on *Patr-1*, a member of the "diffuse" class and a known critical nucleator of P-
218 bodies in other systems (Coller and Parker, 2005; Nissan et al., 2010; Pilkington and
219 Parker, 2008; Pradhan et al., 2012; Sachdev et al., 2019; V et al., 2011). Using a
220 verified antibody (Pradhan et al., 2012), we found PATR-1, like other mRNP proteins,
221 was almost exclusively detected in the cytoplasm of progenitor cells and displayed a
222 distinctive granular organization (**Fig. 2C, 2C'**). PATR-1 also showed a strong but less
223 punctate expression in ~45% of EEs (compare **Fig. S1C-D** to **Fig. 2C''**). PATR-1
224 colocalized well with both TRAL and Me31B (**Fig. S2I-J, L-M**) and did not colocalize
225 with the IPSG protein FMRP (**Fig. S2K, N**), indicating it was a P-body component. We
226 therefore used the PATR-1 antibody as an independent marker to verify the effects of
227 the 103 genes identified above on P-body morphology and found analogous effects in
228 all cases except for the "No TRAL" category (**Fig. S2O-T**). In this class, smaller than
229 normal PATR-1 granules were observed (**Fig. S2T**), suggesting that the identified genes
230 altered overall P-body morphology rather than specifically just TRAL staining.
231 Collectively, these data indicated that PATR-1 was a P-body component in intestinal
232 progenitor cells of adult *Drosophila*.
233 To test whether PATR-1 was required for the recruitment of P-body proteins in
234 addition to TRAL, we first verified that *Patr-1* RNAi eliminated PATR-1 protein
235 expression (**Fig. 2D**) and then analyzed the effect of *Patr-1* RNAi on EDC3, GE-1 and

236 Me31B distribution. The prominent punctate pattern and colocalization of these proteins
237 was lost after *Patr-1* RNAi (**Fig. 2E-O**) indicating a failure in P-body assembly as well as
238 P-body protein interaction. To verify these RNAi phenotypes, we generated a new
239 series of *Patr-1* null alleles that were homozygous lethal, died as third instar larvae,
240 displayed the same lethal phase when in *trans* to a deficiency, and lacked PATR-1
241 protein by Western blot (**Fig. S3A-B**). Using two representative alleles , *Patr-1*$^{P105\Delta}$ and
242 *Patr-1*^{R107FS1}, we then generated *Patr-1* mutant adult progenitors with the Mosaic
243 Analysis with a Repressible Cell Marker (MARCM) technique (Lee and Luo, 1999).
244 Seven days after clone induction, intestines were dissected and either stained for
245 PATR-1 or scored for P-body morphology based on Me31B and EDC3 distribution.
246 PATR-1 staining was not detected in either *Patr-1*$^{P105\Delta}$ or *Patr-1*^{R107FS1} homozygous
247 mutant cells (**Fig. S3C-D**) and a previously verified rescue transgene, *P21M20*
248 (Pradhan et al., 2012), restored PATR-1 staining to *Patr-1*$^{P105\Delta}$ mutant cells (**Fig. S3E**).
249 Similar to *Patr-1* RNAi, the P-body localization of Me31B and EDC3 was completely
250 disrupted in *Patr-1*$^{P105\Delta}$ and *Patr-1*^{R107FS1} mutant clones (**Fig. S3F-G** and **I-J**), and these
251 defects were rescued entirely by the *P21M20* transgene (**Fig. S3H** and **K**). Taken
252 together, these data indicated that PATR-1 was required for P-body assembly in the
253 cytoplasm of adult *Drosophila* intestinal progenitor cells.
254
255 **Loss of PATR-1 leads to progenitor cell loss**
256 To analyze the effects of P-body loss on progenitor cell biology, we crossed
257 control and *Patr-1* RNAi strains to *esgTS* and analyzed intestines for an effect on the
258 total number of cells as well as the number of either progenitors, EEs, or ECs at three
259 timepoints (**Fig. 3A**). Intestinal progenitor cell number in *Patr-1* RNAi intestines
260 gradually declined over time and was almost completely absent after 15 days of RNAi
261 (**Fig. 3B, F-I**). In contrast, EE cell percentage remained unchanged at early time points
262 and showed a slight increase at 15 days (**Fig. 3C**). In addition, EC percentage
263 increased over time and showed ~30% increase at 15 days (**Fig. 3D**). However, the
264 total number of cells per field was significantly reduced at 15 days (**Fig. 3E**), at least in
265 part reflecting the loss of progenitor cells. Consistent with these results, *Patr-1*$^{P105\Delta}$ and
266 *Patr-1*^{R107FS1} mutant clones were smaller and contained fewer ISCs compared to control

267 (**Fig. S3L-R**); these defects were rescued entirely by the *P21M20* transgene. To further
268 validate the loss of mitotic cells in the absence of PATR-1, we fed control and flies
269 expressing *Patr-1* RNAi (14 days) for 1 day with bleomycin, a chemical that induces
270 rapid ISC proliferation due to EC damage, and quantified mitotic proliferation by staining
271 for phosphorylated-histone 3 (pH3), a highly specific marker for condensed
272 chromosomes during mitosis (Amcheslavsky et al., 2009). Consistent with progenitor
273 cell loss, intestines expressing *Patr-1* RNAi for 15 days displayed significantly reduced
274 numbers of pH3 positive cells (**Fig. S3S**). Taken together, these data suggested that
275 progenitor cells were lost and the epithelial integrity was compromised due to a failure in
276 P-body assembly.
277 Given that P-bodies were present in both ISCs and EBs, we assessed whether
278 P-body function was necessary in each cell type by performing knockdown of *Patr-1*
279 using conditional, cell type specific GAL4 drivers, denoted as ISC^{TS}- and EB^{TS}-*GAL4*
280 respectively (Buddika et al., 2020b; Zeng et al., 2010). Consistent with *esg-GAL4* based
281 knockdown, knocking down *Patr-1* in ISCs for 15 days led to a marked reduction in GFP
282 positive ISCs (**Fig. 3J-K)** as well as the complete absence of pH3 positive cells after
283 bleomycin feeding (**Fig. 3L**). Thus, the few surviving ISCs had lost the proliferative
284 potential that wild type ISCs possess. In contrast to the requirement of *Patr-1* for ISC
285 maintenance, knocking down *Patr-1* using the EB^{TS}-*GAL4* had no notable effect on GFP
286 positive EB cell number compared to control after 15 days at permissive temperature
287 (**Fig. 3M-N**). However, *Patr-1* knockdown in EBs resulted in both a marked increase in
288 ISC proliferation (**Fig. 3O**) as well as the emergence of a weakly GFP positive EC-like
289 polyploid cell population (**Fig. 3M**, right). These observations suggested that *Patr-1* loss
290 caused both an increase in the rate of EB differentiation and a commensurate increase
291 in the rate of ISC proliferation that maintained EB number at normal levels. Taken
292 together, these results indicated that *Patr-1* was required to maintain ISCs and limit the
293 rate of EB differentiation.
294
295 **PATR-1 represses pro-differentiation genes in intestinal progenitors**
296 To identify P-body dependent mRNAs whose misregulation might be the
297 underlying cause of the progenitor cell loss described above, we performed

298 transcriptomic profiling (RNA-seq) of FACS (fluorescent activated cell sorting) isolated
299 *Patr-1* RNAi and control intestinal progenitor cells (**Fig. 4A**, **S4A**). *Patr-1* knockdown in
300 intestinal progenitors significantly altered the expression of 1,226 transcripts (**Fig. 4B**,
301 **Table S2**); 703 were upregulated and 523 were downregulated including, most
302 significantly, *Patr-1* mRNA (**Fig. 4B-D**, **Table S2**). Because P-body regulated mRNAs
303 tend to be longer and have a lower GC content than average (Courel et al., 2019), we
304 evaluated the misregulated genes for these characteristics: upregulated genes (3336.1
305 ± 143.9 bp; 44.1 ± 0.2 %) were significantly longer and had a lower GC content than
306 unchanged genes (2698.4 ± 27.7 bp; 46.1 ± 0.1 %) (**Fig. S4B**). Gene Ontology (GO)
307 analysis showed that cell differentiation genes were significantly upregulated, in
308 agreement with the identities of mRNAs found in HEK293 P-bodies (Hubstenberger et
309 al., 2017) (**Fig. S4C**). Since the expression of key pro-apoptotic and -EE fate mRNAs
310 were unchanged (**Fig. S4D-E**, **Table S2**), this transcriptomic analysis suggested that
311 *Patr-1* mutant progenitor cells were lost due to elevated differentiation caused by
312 inappropriate expression of pro-EC fate genes. Similar effects on EC genes have
313 previously been associated with phenotypes caused by loss of other progenitor genes,
314 including the Snail family transcription factor Escargot (Esg) and its co-factor Verthandi
315 (Vtd or Rad21) (Khaminets et al., 2020; Korzelius et al., 2014). Notably, 22% (92/410
316 genes) and 18% (80/454 genes) of the significantly upregulated genes in *esg*-RNAi and
317 *vtd*-RNAi overlapped with *Patr-1* RNAi upregulated genes (**Fig. S4F-G**, **Table S2**).
318 These included EC-marker genes such as *nubbin* (*nub*, also known as POU-domain
319 protein 1 or *Pdm1*), *Myo61F*, and *big bang* (*bbg*) (Khaminets et al., 2020; Korzelius et
320 al., 2014). Taken together, these results suggested that Esg/Vtd and *Patr-1*
321 transcriptionally and post-transcriptionally repress an overlapping cohort of pro-EC
322 genes.
323
324 **PATR-1 limits cytoplasmic *nub* mRNA levels in progenitor cells**
325 To evaluate the relationship between transcriptional and post-transcriptional
326 regulation in progenitor cells, we focused on the *nub* mRNA, which we confirmed via
327 real-time quantitative PCR (qPCR) was upregulated in FACS-isolated *Patr-1* mutant
328 cells (**Fig. 4E-F**). This qPCR analysis, however, detected low levels of *nub* in wildtype

329 intestinal progenitors, suggesting that repression of these transcripts in wildtype
330 progenitors was incomplete. This qPCR result was consistent with low levels of *nub* and
331 other pro-differentiation genes including *bbg* detected by RNA-seq analysis of wildtype
332 progenitors (**Fig. 4D**). To directly confirm these observations, we analyzed the
333 subcellular distribution and levels of *nub* transcript in wildtype intestines using
334 RNAscope *in situ hybridization* probes. As expected, *nub* transcript was readily detected
335 in ECs in both the cytoplasm as well as in bright nuclear punctae that we interpreted as
336 sites of active transcription (**Fig. 4H**, yellow arrowheads). In addition, *nub* transcript was
337 more weakly detected in the cytoplasm of ~33% wildtype progenitor cells, with low-to-no
338 signal in the nuclei of these cells (**Fig. 4H**). In comparison, the *nub* protein product
339 Pdm1, was rarely detected in only ~3% of wildtype progenitors (**Fig. 4J,** quantified in
340 **5A)**. These results indicated that the transcriptional repression of *nub* was incomplete
341 and that a post-transcriptional mechanism ensured the absence of Pdm1 protein in
342 wildtype progenitor cells.
343 To analyze the role of P-bodies in this process, we also analyzed *nub* mRNA and
344 Pdm1 protein patterns and levels in intestinal progenitor cells after *Patr-1* knockdown. In
345 comparison to wildtype progenitors, cytoplasmic *nub* mRNA staining was considerably
346 higher in ~63% *Patr-1* deficient intestinal progenitors (**Fig. 4I**). Only 40% subset of the
347 *Patr-1* mutant progenitor cells with elevated cytoplasmic staining also displayed bright
348 nuclear punctae (**Fig. 4I**, white arrowhead), indicating that elevated cytoplasmic
349 expression did not require nuclear expression. Furthermore, neither *esg* nor *vtd*
350 expression levels were affected by *Patr-1* loss (**Fig. S4H-I**), suggesting that
351 transcriptional repression was unlikely to be compromised by P-body loss. In addition,
352 the number of progenitor cells expressing Pdm1 protein was significantly enhanced
353 after *Patr-1* RNAi (**Fig. 4K,** quantified in **5A**). Collectively, these observations indicated
354 that PATR-1 mediated P-body assembly in progenitor cells was required to limit the
355 stability and translation of pro-differentiation genes such as *nub*.
356
357 **Loss of P-body assembly promotes progenitor-EC differentiation**
358 The elevated Pdm1 protein and transcript levels detected in *Patr-1* mutant
359 progenitor cells suggested that P-body loss caused premature progenitor-to-EC

360 differentiation. Consistently, forced expression of Pdm1 in progenitor cells also led to
361 progenitor cell loss (**Fig. 5B).** In addition, prior to their loss, both the cell and nuclear
362 area of *Patr-1* mutant intestinal progenitors was significantly elevated (**Fig. 5C-D**),
363 suggestive of the acquisition of polyploid EC characteristics. Since no increase in GFP+
364 PROS+ cells or apoptotic cell death was observed (**Fig. S5A-C)**, these observations
365 indicated that P-body loss was associated with derepressed translation of pro-
366 differentiation gene products in progenitor cells that led to progenitor-to-EC
367 differentiation and consequent progenitor cell loss. Consistently, we noted that feeding
368 adults bleomycin, which leads ISCs to rapidly proliferate, differentiate and upregulate
369 Pdm1 (Tian et al., 2017), was also associated with P-body dissolution (**Fig. S5D-I**).
370 Taken together, these data showed that P-bodies are required for progenitor cell
371 maintenance by suppressing EC-fate.
372
373 **Overexpression of *esg* rescues *Patr-1* RNAi mediated progenitor cell loss**
374 The presence of *nub* transcript but absence of Pdm1 protein in progenitor cells
375 suggested that P-bodies limited the translation of weakly transcribed pro-differentiation
376 genes to maintain progenitor cell identity. To test whether the overexpression of *esg*,
377 which we hypothesized would block this weak transcription, eliminated the requirement
378 of mature P-body formation to prevent differentiation, we analyzed the effects of
379 progenitor expression of UAS-*Patr-1* RNAi and UAS-*esg* transgenes, both individually
380 and in combination, on progenitor cell numbers. Consistent with our previous
381 observations, knocking down *Patr-1* significantly reduced the number of intestinal
382 progenitors while *esg* overexpression significantly increased the progenitor cell number
383 (**Fig. 5B, S5J**). However, the ectopic expression of Pdm1 and ensuing progenitor cell
384 loss associated with *Patr-1* knockdown was eliminated when *esg* was simultaneously
385 expressed (**Fig. 5A-B, S5J-K**). We verified this at the mRNA level with both qPCR and
386 RNAscope analysis. As expected, *esg* but not *Patr-1* transcript abundance was
387 significantly elevated in progenitors expressing UAS-*esg* (**Fig. 4E, G**). Consistent with
388 our model, this ectopic *esg* expression significantly reduced *nub* mRNA level in both
389 wildtype and *Patr-1* mutant progenitor cells (**Fig. 4F, 5E-F**). To verify that the rescued
390 progenitor cells in the UAS-*Patr-1* RNAi/UAS-*esg* background included bona fide ISCs,

391 we assessed the mitotic potential of intestines of each of the above genetic
392 backgrounds following bleomycin feeding. As expected, overexpression of *esg* in *Patr-1*
393 deficient intestinal progenitors elevated the total number of mitotic ISCs (**Fig. 5G**).
394 However, mature P-bodies were not restored, as indicated by diffuse TRAL staining in
395 these intestinal progenitors (**Fig. S5L**). Taken together, enhanced transcriptional
396 repression of pro-differentiation genes associated with *esg* overexpression can prevent
397 premature progenitor differentiation independent of mature P-body assembly.
398

399 ## Discussion

400 This study molecularly and functionally characterized stem cell mRNPs that we
401 conclude are P-bodies based on three observations: (i) they contain colocalized protein
402 complexes that include fly orthologs of proteins known to localize to P-bodies in
403 mammalian and yeast cells, (ii) these mRNP granules are significantly larger than and
404 show no colocalization with IPSG protein foci under controlled conditions, and (iii) acute
405 stresses increase the size of these mRNPs and promotes colocalization with IPSGs. A
406 targeted genetic screen identified 103 genes, 39 previously known and 64 novel
407 candidates, that can influence P-body morphology, including six that are required for P-
408 body formation. To examine stem cell P-body function, we genetically characterized one
409 of these latter class, PATR-1, an evolutionary conserved protein with both translational
410 repression and mRNA decay functions that is necessary for proper P-body assembly in
411 *Saccharomyces cerevisiae* (Coller and Parker, 2005; Eulalio et al., 2007b; Scheller et
412 al., 2007; Sheth and Parker, 2003; Teixeira and Parker, 2007) (Pilkington and Parker,
413 2008; Sachdev et al., 2019). Genetic depletion of P-bodies in progenitor cells
414 upregulated the expression of pro-differentiation genes such as *nubbin*, which was
415 weakly transcribed but translationally repressed in wildtype progenitor cells. Loss of
416 stem cell P-bodies, either by genetic depletion or differentiation, led to the increased
417 translation as well as the cytoplasmic, but not nuclear, abundance of such transcripts.
418 We therefore concluded that mature P-bodies are necessary for stem cell maintenance
419 by post-transcriptionally enforcing the repression of transcriptional programs that
420 promote differentiation. Differentiation signals dissolve P-bodies and thereby promote
421 translation of target differentiation genes (**Fig. 6**).

422 Since detailed ultrastructural organization of P-bodies has been lacking (Youn et
423 al., 2019), we used quantitative super-resolution microscopy-based characterization to
424 show substructures present within mature P-bodies. Consistent with the proposed
425 "core-shell" structure of stress granules (Jain et al., 2016; Niewidok et al., 2018;
426 Wheeler et al., 2016; Youn et al., 2019), P-bodies exhibit "cores" with high protein
427 concentrations and "shells" with low protein concentration. Notably, Drosophila intestinal
428 progenitor P-bodies have a diameter of ~125 nm, as compared to the larger P-bodies in
429 HEK293 cells, which have a ~500 nm diameter (Hubstenberger et al., 2017). In addition,

430 intestinal progenitors contain ~35-45 mature P-bodies while HEK293 cells contain only
431 ~4-7 granules per cell. This indicates that the size and the number of mature P-bodies
432 depends on cell type and species and may scale based on overall cell size.
433 A recent study documented the presence of P-bodies in cultured human
434 pluripotent stem cells (hPSCs) and suggested their presence in adult stem cells (Di
435 Stefano et al., 2019). This analysis of DDX6, the ortholog of *Drosophila* Me31B, showed
436 that DDX6-dependent P-bodies could both promote and repress stem cell identity,
437 depending on context. For example, loss of DDX6 expanded endodermally derived
438 Lgr5^{+} ISC or ectodermally derived neural progenitor cell populations, but promoted the
439 differentiation of other progenitor cell populations, including mesodermally derived
440 progenitors. We confirm the presence of mature P-bodies in adult progenitor
441 populations but show that they repress differentiation rather than increasing their
442 proliferation, as in Lgr5^{+} ISCs. A few possible explanations could explain these results.
443 Most simply, *Drosophila* intestinal progenitors behave more like mesodermally derived
444 mammalian progenitors rather than endo- or ectodermally derived mammalian
445 progenitors. Alternatively, the stem cell function of DDX6 might be affected by its roles
446 in surrounding cells, since DDX6 was targeted in cells throughout mouse intestinal
447 organoids, whereas PATR-1 was specifically targeted only in progenitor cells in our
448 study. Finally, DDX6-mediated P-body function might be modulated by signaling that is
449 not fully recapitulated in *in vitro*-derived stem cell models.
450 The exact molecular function of P-bodies is a matter of current debate (Sachdev
451 et al., 2019). While earlier models proposed that the primary function of P-bodies was
452 mRNA degradation, more recent findings propose that P-bodies function as sites of
453 mRNA storage and control the translatome of cells (Anderson and Kedersha, 2006;
454 Decker and Parker, 2012; Standart and Weil, 2018). While our RNA-seq analysis
455 identifies potential targets of P-bodies, more direct approaches such as enhanced-CLIP
456 (eCLIP) (Van Nostrand et al., 2016) of P-body proteins driven with recently developed
457 progenitor specific *I-KCKT-GAL4* drivers (Buddika et al., 2020b) will be used in the
458 future to directly profile the P-body transcriptome of intestinal progenitors. Our data,
459 however, suggest that intestinal progenitor P-bodies may have both translational
460 repressive and mRNA degratory functions. We found that the *nub* mRNA was weakly

461 expressed but not translated in wildtype intestinal progenitors, and that this translational
462 repression was P-body dependent. In addition, the abundance of EC-specific transcripts
463 was influenced by P-bodies in a transcription independent fashion: RNAscope *in situ*
464 analysis showed that the cytoplasmic *nub* transcript abundance was increased in *Patr-1*
465 mutant progenitor cells without an indication of nuclear transcription. Therefore, this
466 PATR-1 dependent increase in cytoplasmic *nub* mRNA could be attributed to the
467 stabilization of transcripts that are targeted for degradation via P-bodies. Consistently,
468 studies of P-bodies and P-body proteins in human cultured stem cells also sugget dual
469 roles in both mRNA translation repression and degradation. For instance, P-bodies
470 influence the translation of transcripts encoding fate-instructive transcription and
471 chromatin factors in cultured embryonic and *in vitro*-derived adult stem cells (Di Stefano
472 et al., 2019). In addition, P-body proteins DDX6 and EDC3 are known to destabilize
473 differentiation-inducing mRNAs such as KLF4 in human epidermal progenitor cells,
474 although it is important to note that P-bodies have not been reported in these cells
475 (Wang et al., 2015).
476 Based on our data, the weak transcription of pro-differentiation genes likely
477 maintains progenitor cells in a primed state where differentiation program can be
478 initiated rapidly and independent of transcription of differentiation genes. The
479 transcriptional repression of differentiation genes by the transcription factor *esg* is a key
480 regulatory step of intestinal stem cell maintenance (Antonello et al., 2015; Khaminets et
481 al., 2020; Korzelius et al., 2014; Li et al., 2017; Liu and Jin, 2017; Loza-Coll et al.,
482 2014). The loss of *esg* gene expression or inability to localize the Esg protein to target
483 genes promote progenitor cell loss via premature ISC-to-EC differentiation (Khaminets
484 et al., 2020; Korzelius et al., 2014). Similar to *Patr-1* RNAi, knocking down *esg* itself as
485 well as either *vtd*, *Nipped-B* or *polo*, all of which are necessary for recruiting Esg to
486 target promoters, markedly upregulated the expression of Pdm1 in intestinal progenitors
487 (Khaminets et al., 2020; Korzelius et al., 2014). Notably, our transcriptomic profiling
488 showed that the transcript level of neither *esg* nor any of the Esg-targeting proteins, *vtd*,
489 *Nipped-B* or *polo*, was changed by the absence of mature P-bodies. These
490 observations suggest that Esg protein level, its proper promoter targeting, and its

491 transcriptional repression of EC-genes are all unlikely to be affected by the loss of
492 PATR-1.
493 In addition to identifying 64 new genes affecting P-body morphology, we expect
494 that the tissue-based stem cell P-body system identified and described here will prove
495 critically useful in screening for chemicals, diet conditions and stress conditions that
496 alter P-body assembly as well as performing larger, genome-wide screens to
497 comprehensively characterize the molecular pathways that control P-body assembly.
498 Moreover, similar approaches can be used to identify systemic signals that promotes P-
499 body disassembly during the onset of differentiation as well as to identify molecular
500 players of P-body disassembly.

Acknowledgements

We thank Scott Barbee, Anne Ephrussi, Xiaohang Yang, the Bloomington *Drosophila* Stock Center (supported by grant NIHP4OOD018537), the *Drosophila* Genome Resource Center (supported by grant NIH2P40OD010949), and the Developmental Studies Hybridoma Bank (created by the NICHD of the NIH) for reagents; Robert Policastro for bioinformatics expertise; the Light Microscopy Imaging Center (supported by grant NIH1S10OD024988-01) for access to the SP8 confocal and OMX super-resolution microscopes; the Flow Cytometry Core Facility at Indiana University, Bloomington for access to the BD FACSAria™ II flow cytometer; and the National Institute of General Medical Sciences (Award R01GM124220) for financial support.

Declaration of Interests

The authors declare no competing interests.

515 ## Figures and Figure Legends

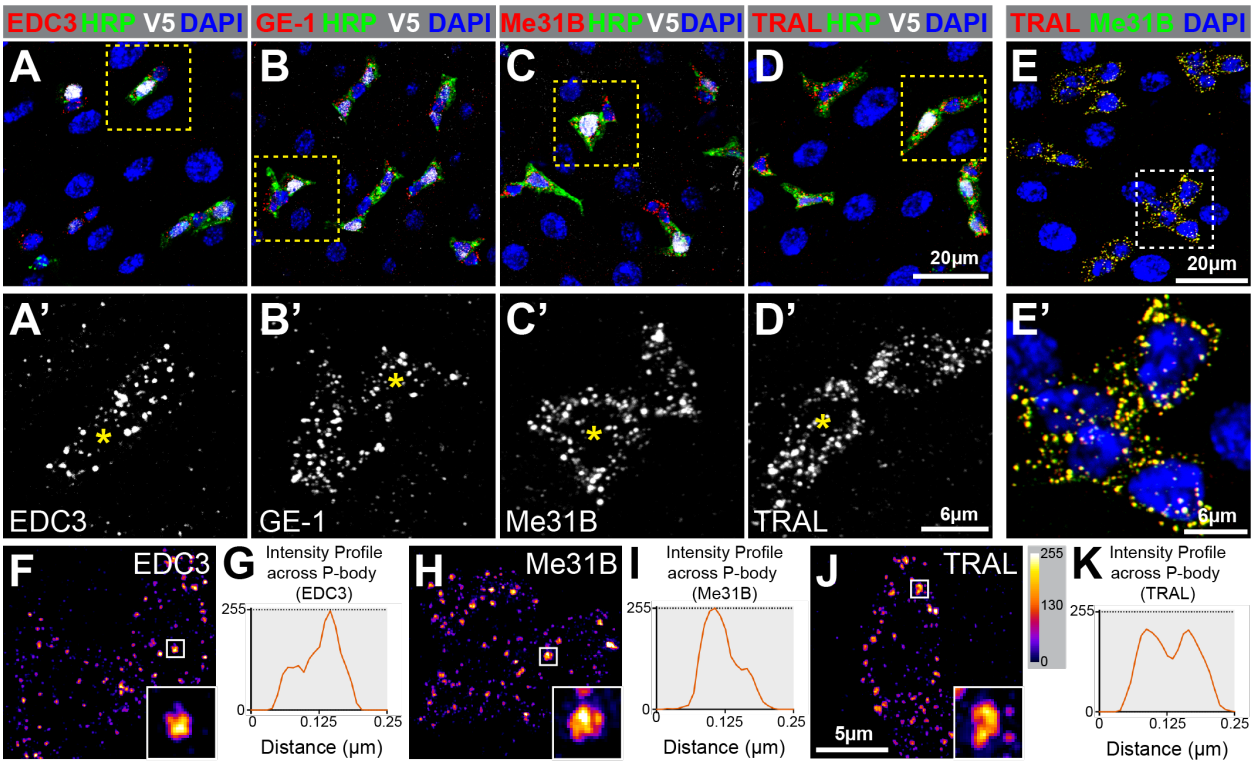

516

517 **Figure 1:** Intestinal progenitor cells contain P-bodies. (A-D) Adult posterior midguts
518 stained in red for (A) EDC3, (B) GE-1, (C) Me31B, and (D) TRAL. *3Xgbe-*
519 *smGFP::V5::nls* (white) labels EBs, HRP (green) labels both EBs and ISCs, and the
520 DNA-dye DAPI (blue) labels all cells. A'-D' are enlargements of progenitor cells
521 indicated in A-D with EBs labeled (asterisks). (E) Adult posterior midgut stained for
522 TRAL (red), Me31B (green), and DAPI (blue). (F, H, J) Super-resolution micrographs of
523 progenitor cells stained for (F) EDC3, (H) Me31B, or (J) TRAL and pseudocolored using
524 scale in J to indicate protein level. Insets are enlarged views of boxed regions. (G, I, K)
525 Line plots showing pixel-by-pixel intensity profiles of insets.

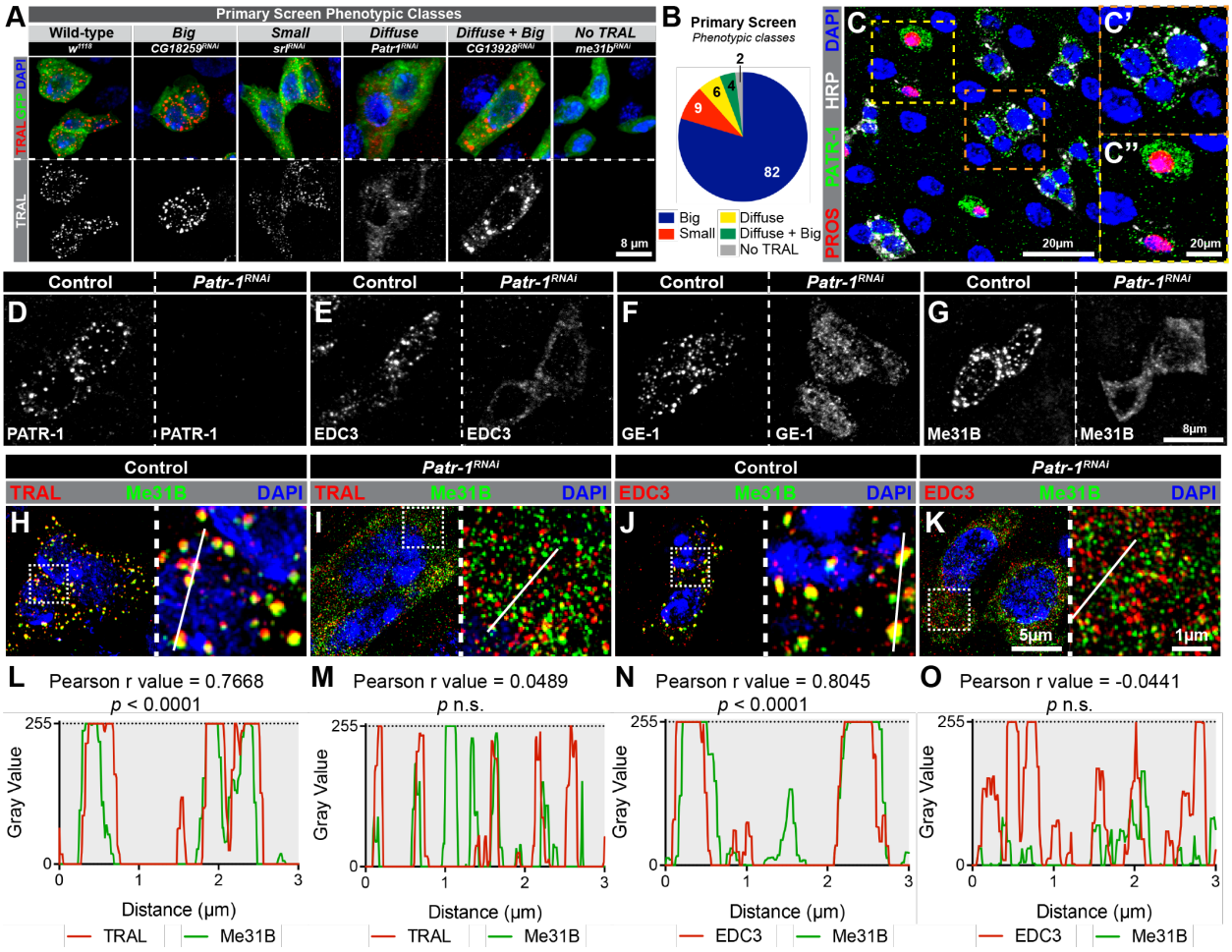

Figure 2: RNAi screen identifies PATR-1 as an essential component of progenitor cell P-bodies. (A) Examples of the five classes of P-body phenotypes showing progenitor cells from *esg*^{TS}, *esg*^{TS} / *CG18259* RNAi, *esg*^{TS} / *srl* RNAi, *esg*^{TS} / *Patr-1* RNAi, *esg*^{TS} / *CG13928* RNAi, or *esg*^{TS} / *me31b* RNAi intestines stained for TRAL (red), GFP (green), and DAPI (blue). (B) Chart of phenotypic class numbers. (C) Posterior midguts stained for PROS (red), PATR-1 (green), HRP (white) and DAPI (blue). C' and C'' are enlargements of regions indicated in C. (D-G) Progenitor cells from *esg*^{TS} (control, left) or *esg*^{TS} / *Patr-1* RNAi (right) intestines stained for (D) PATR-1, (E) EDC3, (F) GE-1, or (G) Me31B. (H-K) Super-resolution micrographs of (H, J) *esg*^{TS} or (I, K) *esg*^{TS} / *Patr-1* RNAi intestinal progenitors stained for Me31B (green), DAPI (blue) and either TRAL (red in H, I) or EDC3 (red in J, K). (L-O) Normalized pixel-by-pixel fluorescent intensity profiles of indicated protein (TRAL, Me31B or EDC3) along white lines in H-K.

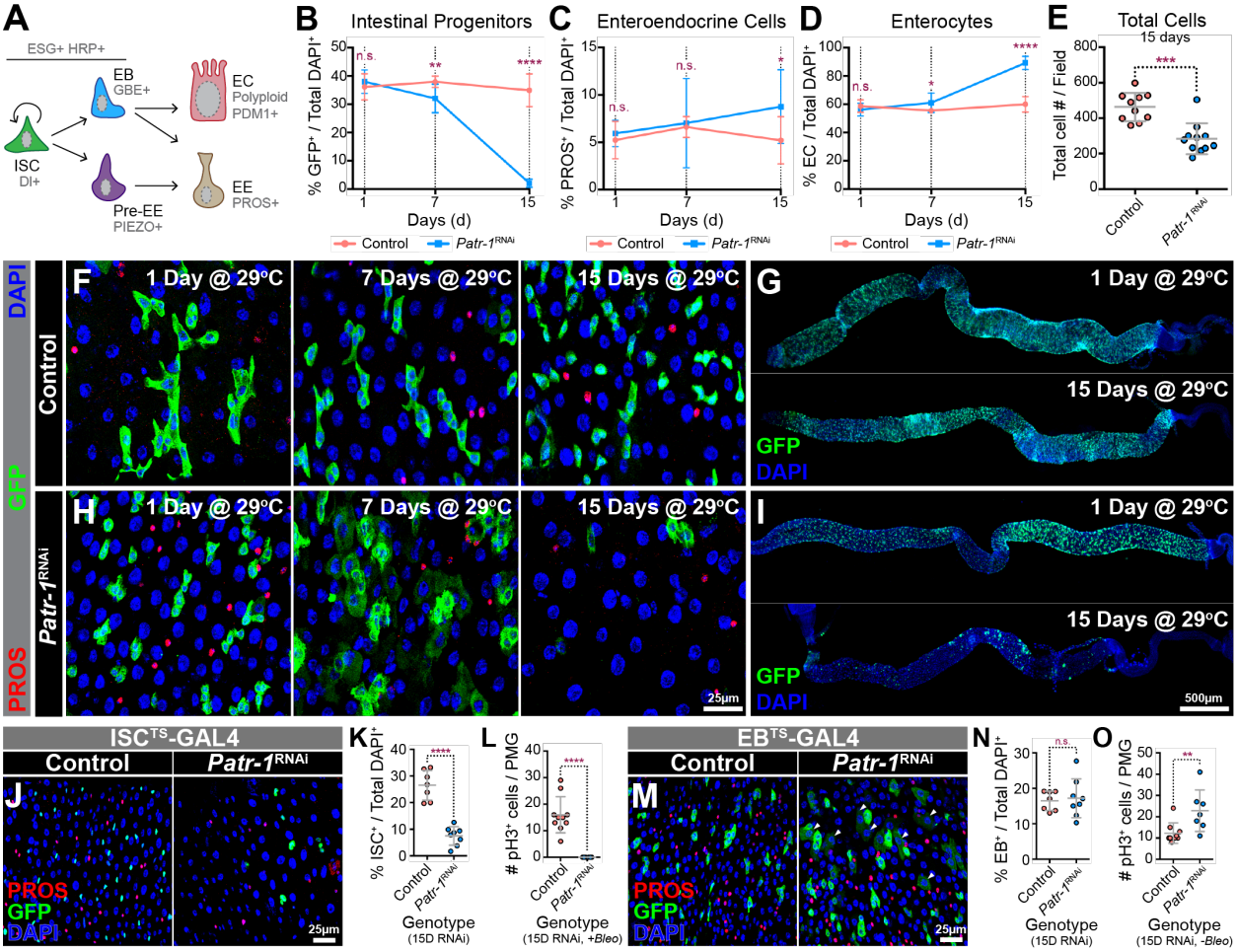

Figure 3: PATR-1 maintains intestinal progenitor cells. (A) Schematic of intestinal cell types and markers. (B-D) Normalized (B) intestinal progenitor cell, (C) EE cell, or (D) EC percentages in *esg*^{TS} (pink) and *esg*^{TS} / *Patr-1* RNAi (blue) posterior midguts (n=8-to-11) after 1, 7 and 15 days at 29°C. (E) Dot-plot of total cell number per field of view in *esg*^{TS} (n=10) and *esg*^{TS} / *Patr-1* (n=11) midguts after 15 days at 29°C. (F, H) Sections from (F) *esg*^{TS} or (H) *esg*^{TS} / *Patr-1* RNAi midguts after 1, 7 and 15 days at 29°C stained for PROS (red), GFP (green) and DAPI (blue). (G, I) *esg*^{TS} (G) and *esg*^{TS} / *Patr-1* RNAi (I) intestines after 1 and 15 days at 29°C stained for GFP (green) and DAPI (blue). (J) Sections from *ISC-KCKT-GAL4*^{TS} (left) or *ISC-KCKT-GAL4*^{TS} / *Patr-1* RNAi (right) midguts after 15 days at 29°C stained for PROS (red), GFP (green) and DAPI (blue). (K-L) Normalized ISC percentage (n=7 or 8) or number of pH3+ cells per posterior midgut after bleomycin feeding (n=10 or 7) of genotypes shown in J. (M) Sections from *gbe*^{TS} (left) or *gbe*^{TS} / *Patr-1* RNAi (right) 15 days after shifting to 29°C and stained for PROS

553 (red), GFP (green) and DAPI (blue). (N-O) Normalized EB percentage (n=7 or 8) or the
554 total number of pH3+ mitotic cells per posterior midgut (n=9 or 7) without bleomycin
555 feeding of genotypes shown in M. Error bars on plots show mean±s.d. and asterisks
556 denote statistical significance from Unpaired t-test (B-D, K, N-O) or Mann-Whitney test
557 (E, L). *p <0.05; **p < 0.01; ***p < 0,001; ****p < 0.0001; n.s., not significant.

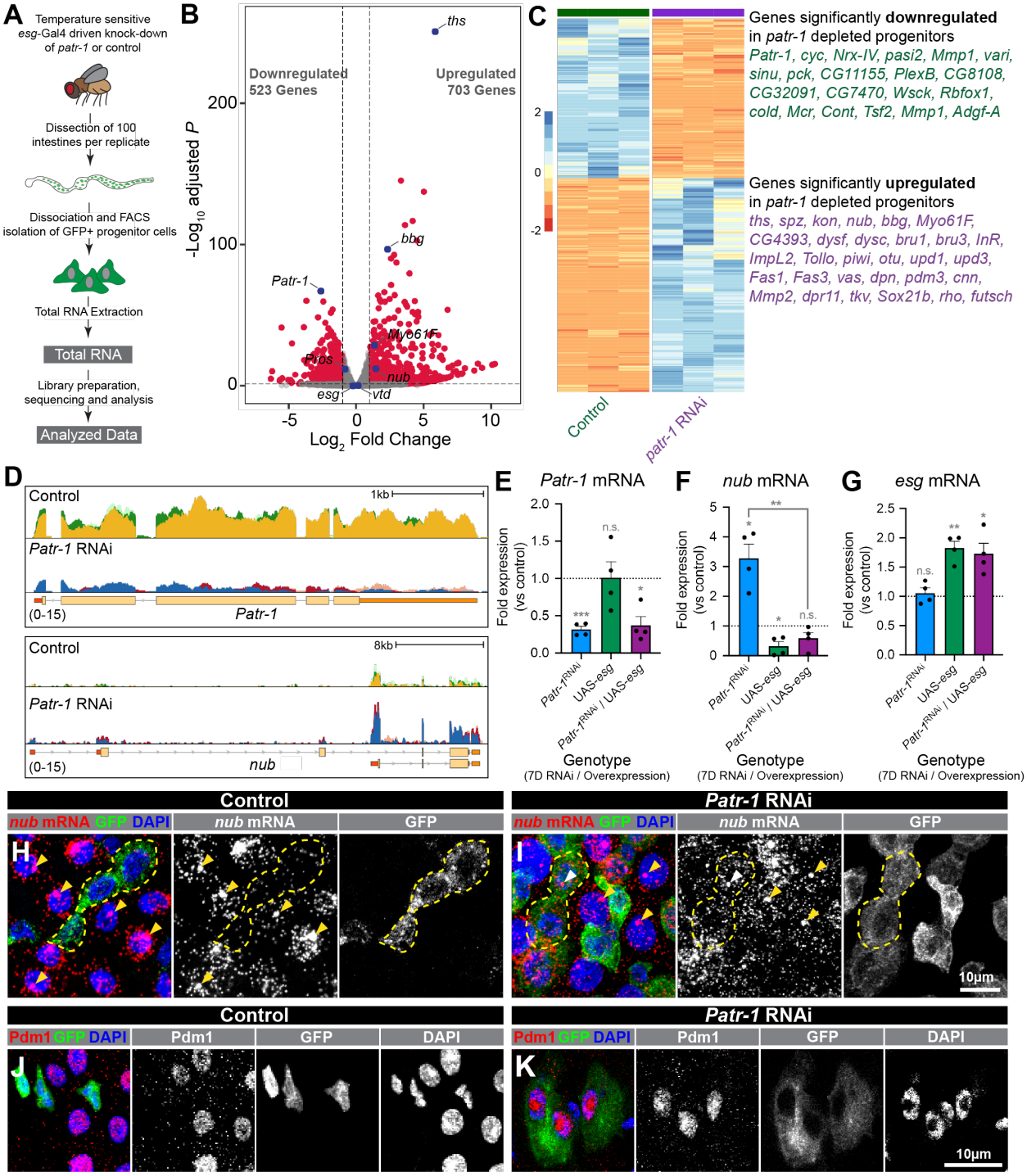

Figure 4: PATR-1 limits pro-differentiation gene expression in intestinal progenitor cells. (A) Schematic of RNA-seq analysis. (B) Volcano plot of differentially expressed genes in *Patr-1* RNAi versus control. Each dot represents a single gene. Red indicate a false discovery rate (FDR) adjusted p-value < 0.05 and a Log_2 fold change > 1 or < -1. (C) Heatmap showing differentially expressed genes (FDR < 0.05; Log_2 fold change > 1 or

564 < -1) in *Patr-1* RNAi versus control with a selected set of gene names shown. (D)
565 Genome browser tracks of CPM-normalized reads from control and *Patr-1* RNAi at the
566 *Patr-1* and *nub* loci. Replicates of control (yellow, light green and dark green) and *Patr-1*
567 RNAi (blue, pink and red) have been overlayed. (E-G) Fold expression of (E) *Patr-1*, (F)
568 *nub*, and (G) *esg* mRNA in intestinal progenitors of esg^{TS} / *Patr-1 RNAi*, esg^{TS} / *UAS-esg*
569 and esg^{TS} / *Patr-1 RNAi* / *UAS-esg* compared to esg^{TS} as determined by qPCR. Error
570 bars show mean±s.d. and asterisks denote statistical significance from one sample t
571 and Wilcoxon test *$p < 0.05$; **$p < 0.01$; n.s., not significant. (H-K) Intestinal progenitors
572 from (H, J) esg^{TS} and (I, K) esg^{TS} / *Patr-1 RNAi* stained for (H-I) *nub* mRNA (red) or (J-
573 K) Pdm1 (red) and GFP (green) and DAPI (blue). Yellow dotted outline on H-I marks
574 intestinal progenitor cells. Yellow and white arrowheads on H-I mark nuclear staining
575 that we interpret as active transcription in ECs and progenitors, respectively.

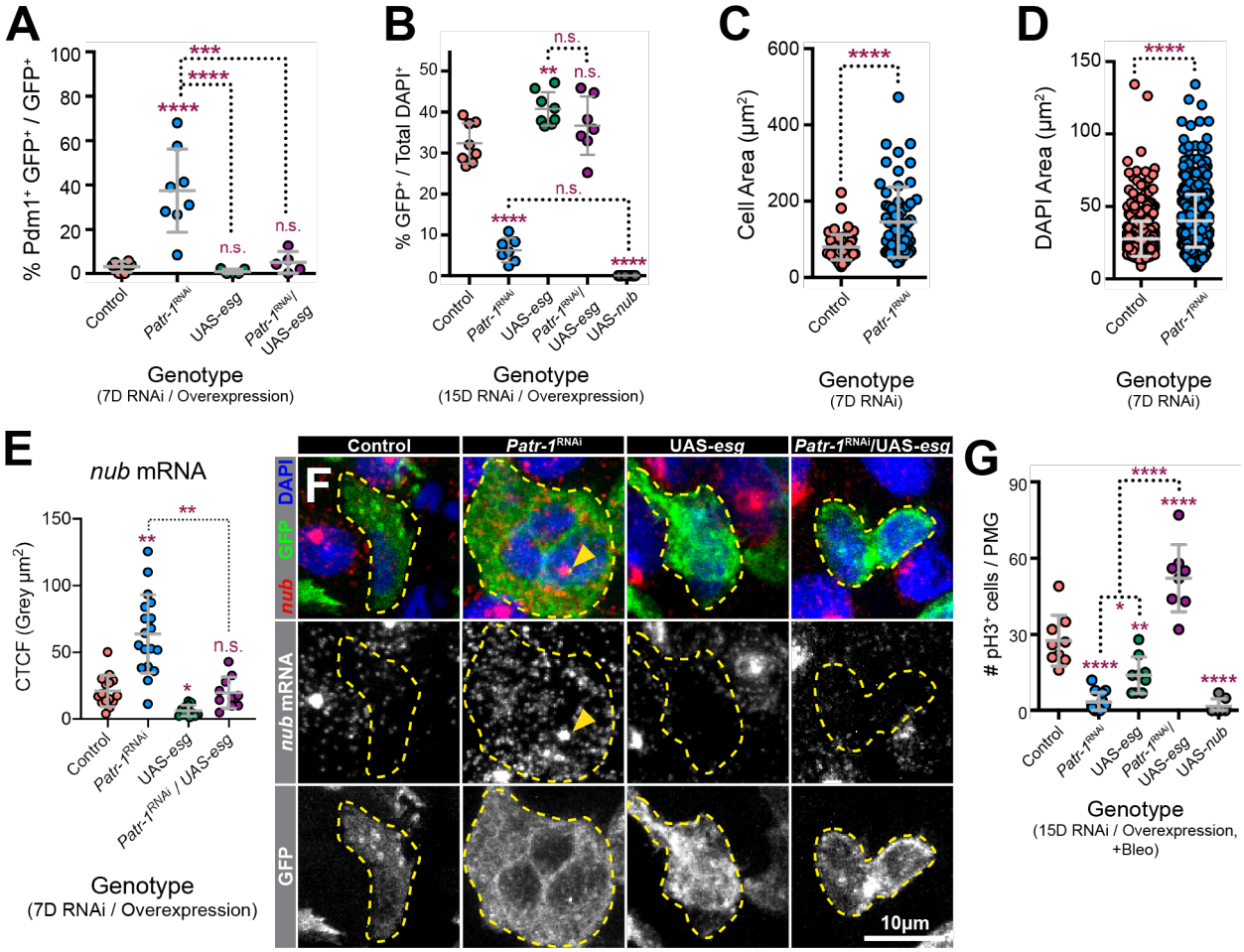

Figure 5: Loss of PATR-1 promotes progenitor-to-EC-differentiation. (A-E) Dot-plots showing (A) percentage of intestinal progenitors with nuclear Pdm1 staining (n=6, 8, 5, or 5), (B) normalized intestinal progenitor cell percentage (n=8, 7, 8, 7, or 8), (C) cell area (n=58 or 61), or (D) nuclei area (n=717 or 619) of indicated genotypes after (A, C, D) 7 or (B) 15 days at 29ºC. (E) Dot plot showing the normalized *nub* mRNA fluorescence intensity of progenitor cells from *esg*^{TS} (n=15 cells), *esg*^{TS} / *Patr-1 RNAi* (n=18 cells), *esg*^{TS} / *UAS-esg* (n=12 cells), or *esg*^{TS} / *Patr-1 RNAi* / *UAS-esg* (n=10 cells) intestines. (F) Intestinal progenitors from genotypes in E stained for *nub* mRNA (red), GFP (green) and DAPI (blue). Yellow dotted outline marks intestinal progenitor cells. Yellow arrowhead mark nuclear staining that we interpret as active transcription. (G) Bleomycin-induced pH3+ cell number per posterior midgut (n=9, 14, 9, 8, or 7) of indicated genotypes after 15 days at 29ºC. Error bars on plots show mean±s.d. and asterisks denote statistical significance from Ordinary one-way ANOVA with Turkey's

590 multiple comparison test (A-B, G), Mann-Whitney test (C-D) or Kruskal-Wallis test (E).

591 *$p < 0.05$; **$p < 0.01$; ****$p < 0.0001$; n.s., not significant.

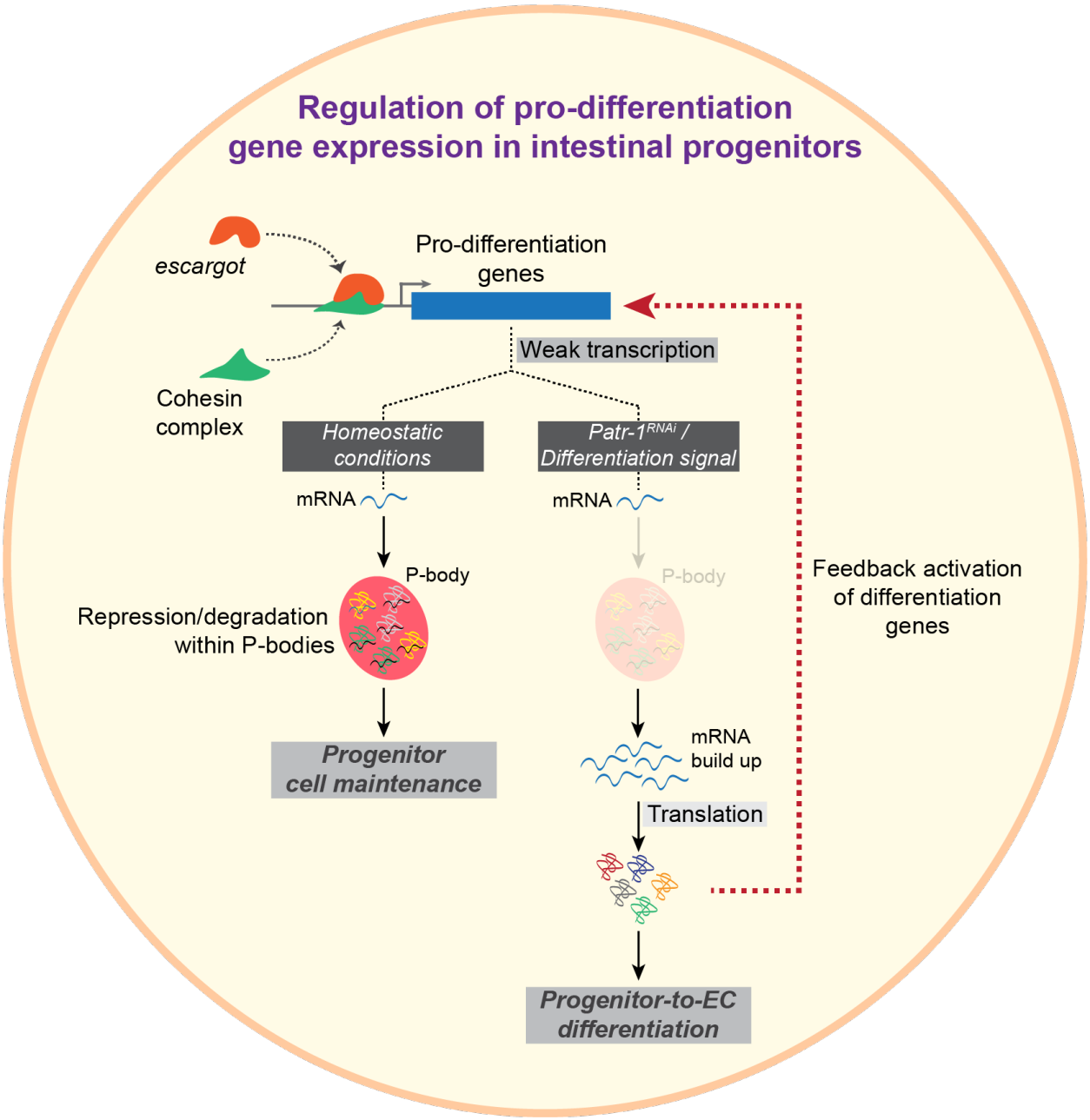

Figure 6: P-body mediated post-transcriptional regulation maintains progenitor cell identity. The model proposing how Patr-1 mediated P-body formation modulate progenitor cell fate.

596 **STAR Methods**

597

598 Key reagents and resources are listed in **Table S3**.

599

600 ***Drosophila strains and husbandry:***

601 Age matched female flies were used in all experiments. Fly strains were cultured on
602 standard Bloomington *Drosophila* stock center media
603 (https://bdsc.indiana.edu/information/recipes/bloomfood.html) and reared in 18°C, 25°C
604 and 29°C incubators set for a 12hr light/dark schedule and 65% humidity. Flies were
605 cultured in groups of 15-20 (typically 5 males and up to 15 females). All strains used in
606 individual panels are listed in **Table S4**.

607

608 ***Temperature:***

609 For temporal and regional gene expression-targeting (TARGET) experiments, flies were
610 grown at 18°C, collected over 2 days, and reared in 29°C for up to 20 days before being
611 dissected. For clonal analysis using mosaic analysis with repressible cell marker
612 (MARCM) method, animals were reared at 25°C until eclosion, collected over 2 days
613 and heat-shocked immediately at 37°C for 45 min in a Lauda circulating water bath.
614 Subsequently, flies were reared at 25°C for 7-15 days.

615

616 ***Construction of new strains:***

617 *CRISPR/cas9 mediated generation of Patr-1 alleles*

618 New *Patr-1* alleles were generated by co-injection of two guide RNA (gRNA) plasmids.
619 The gRNA plasmids were generated by subcloning annealed oligos encoding gRNA 5'-
620 catgttgaacatgttatacatgg-3' as well as annealed encoding gRNA 5'-
621 tgtgacgagactgtcggaagggg-3' into the BbsI site of *pU6-BbsI-chiRNA* (Gratz et al 2013).
622 The two resulting plasmids were sequence-verified, amplified, mixed, and co-injected
623 into strain y^1 *sc** v^1 sev^{21} *; P{nos-Cas9}attP2* (BL78782) by Rainbow Genetics
624 (Camarillo CA). Stocks of F_1 progeny were generated, and strains containing new *Patr-*
625 *1* alleles were selected based on non-complementation of the lethality associated with
626 *P{EPgy2}Patr-1*^{EY10289} (BL19805). New *Patr-1* alleles were molecularly defined by

627 sequencing PCR products generated from genomic DNA obtained from homozygous
628 mutant larvae with oligos flanking the gRNA locations. Two new *Patr-1* alleles as well as
629 *P{EPgy2}Patr-1*^{EY10289} were recombined onto P{FRT}^{82B}-containing chromosomes using
630 standard meiotic methods.
631
632 ***Antibody generation:***
633 Anti-TRAL antibodies were generated in rats (Cocalico Biologicals, Reamstown PA)
634 against a 6XHIS-tagged version of an N-terminal portion of TRAL that was expressed
635 and purified according to standard methods. The TRAL-encoding plasmid was
636 generated by PCR amplifying a 477bp fragment that encodes the first 160 amino acids
637 of TRAL from cDNA GH08269 (DGRC stock 4838) with high-fidelity Q5 polymerase
638 (NEB), subcloning the resulting PCR product into the NcoI and EcoRI sites of
639 pHIS.parallel using HiFi DNA Assembly Master Mix (NEB), and sequence-verifying the
640 resulting plasmid to confirm the absence of any PCR-induced errors.
641
642 Anti-EDC3 antibodies were generated in rabbits and rats (MBL, Japan) against a
643 6XHIS-tagged version of an N-terminal portion of EDC3. The *edc3* coding sequence
644 (corresponding to amino acid 1-440) was PCR-amplified from an ovarian cDNA library
645 using Phusion DNA polymerase (Finnzymes), with primers 5´-
646 GGGAATTCATGGGTCCGACGGATCAAGA-3´ and 5´-
647 GGGGCGGCCGCTCACTTATCGGCACTTATCTCGA-3´. The fragment was digested
648 by *Eco*RI and *Not*I, and cloned into the pProEX HTa vector (Life Technologies). The
649 6×His-tagged Edc3 (1-440) protein was expressed in *E. coli* BL21 cells by IPTG
650 induction, and purified using Ni-NTA agarose resin (Qiagen) under denaturing
651 conditions. The protein was further purified by disc preparative SDS-PAGE using the
652 NA-1800 apparatus (Nihon Eido, Japan). Purified protein fractions were concentrated
653 with Vivaspan-2 (10,000 MWCO PES; Sartorius), dialyzed against PBS containing 4M
654 urea followed by PBS/2M urea. Polyclonal antibodies were affinity-purified with the
655 same antigen immobilized on HiTrap NHS columns (GE Healthcare).
656
657 ***Dissections and immunostaining:***

658 Gastrointestinal (GI) tracts of adult female flies were dissected in ice-cold 1xPBS and
659 fixed in 4% paraformaldehyde (Electron Microscopy Sciences, Cat. No. 15714) in PBS
660 for 45 min. These samples were washed with 1xPBT (1xPBS, 0.1% Triton X-100) and
661 then blocked (1xPBT, 0.5% Bovine Serum Albumin) for at least 45 min. Subsequently,
662 samples were incubated at 4°C overnight with primary antibodies, including rabbit anti-
663 GFP (A11122, Life Technologies, 1:1000), mouse anti-V5 (MCA1360GA, Bio-Rad,
664 1:250), mouse anti-FLAG (F3165, Sigma, 1:1000), rabbit anti-HA (3724S, Cell Signaling
665 Technology, 1:1000), mouse anti-FMR1 (5A11, Developmental Studies Hybridoma
666 Bank, 1:100), mouse anti-Prospero (MR1A, Developmental Studies Hybridoma Bank,
667 1:100), mouse anti-Delta (C594.9B, Developmental Studies Hybridoma Bank, 1:500),
668 rat anti-TRAL (this study, 1:1500), rabbit anti-Me31B (Nakamura A, Amikura R, Hanyu
669 K, 2001) (1:2000), mouse anti-Me31B (Barbee et al., 2006) (1:1500), rabbit anti-Ge-1
670 (Fan et al., 2011) (1:500), rat anti-EDC3 (this study, 1:1500), rabbit anti-EDC3 (this
671 study, 1:2000) and rabbit anti-Pdm1 (a gift from Xiaohang Yang) (1:1500). Samples
672 were washed and incubated for 2-3 hours with secondary antibodies, including
673 AlexaFluor-488 and -568-conjugated goat anti-rabbit, -mouse and -rat antibodies (Life
674 Technologies, 1:1000). AlexaFluor-647 conjugated goat-HRP antibodies were used in
675 the secondary antibody solution whenever required. Samples were washed and treated
676 with DAPI (1:10000) and mounted in Vectashield (Vecta Laboratories). An alternative
677 staining protocol was used for Delta staining as described in Buddika et al., 2020a.
678
679 ***RNAscope in situ hybridization:***
680 Adult female flies were dissected in ice cold 1X PBS and fixed in 4% paraformaldehyde
681 (Electron Microscopy Sciences, Cat. No. 15714) in PBS for 45 min. Tissue was then
682 washed in 1xPBT (1xPBS, 0.3% Triton X-100) 3 times 5 min each. Next, samples were
683 gradually dehydrated with a series of 0.3% PBT (1xPBS, 0.3% Triton X-100): Methanol
684 (7:3, 1:1, 3:7) washes and incubated in Methanol for 10min. Then tissue was rehydrated
685 with a series of 0.3% PBT: Methanol (3:7, 1:1, 7:3) washes and washed with 0.3% PBT
686 alone for another 5 min. For following steps, reagents from RNAscope Multiplex
687 Fluorescent Reagent Kit v2 assay were used. Fixed tissue was transferred into 0.2 ml
688 PCR tubes and incubated in RNAscope Protease III reagent for 5 min at 40°C (PCR

689 thermal cycler was used for all the incubations at 40°C). Samples were immediately
690 washed with 1X PBS twice and 20µl of RNAscope probes for *nub* (pre warmed to 40°C)
691 (ACD Bio., Cat. No. 523981) was added. Samples were incubated at 40°C overnight.
692 After overnight incubation, samples were washed twice with 1X RNAscope wash buffer.
693 Next, RNAscope Multiplex FL v2 AMP 1, RNAscope Multiplex FL v2 AMP 2, RNAscope
694 Multiplex FL v2 AMP 3 and RNAscope Multiplex FL v2 HRP-C1 steps were done as
695 described in Chapter 4 of Fluorescent v2 assay manual, ACD Bio. Finally, samples
696 were incubated for 30 min at 40°C with Opal 620 (AKOYA Biosciences, Cat. No.
697 FP1495001KT, 1:1500 in TSA buffer) and washed with 1X RNAscope wash buffer and
698 counterstained with DAPI. Samples were mounted in ProLong Diamond mounting
699 medium (Invitrogen).
700
701 ***Microscopy and image processing:***
702 Images were collected on either a Leica SP8 Scanning Confocal microscope (Leica
703 DMi8 inverted microscope platform; equipped with WLL 470-670 nm, 405 nm and 440
704 nm lasers, Huygens deconvolution software; controlled by Leica LAS-X software; image
705 acquisition using Leica HC PL APO CS2 63x/1.40 or Leica HC PL APO CS2 40x/1.40
706 lens with Leica Type F Immersion Liquid (N = 1.518)) or an OMX 3D-SIM Super-
707 Resolution microscope (DeltaVision OMX system; equipped with 405, 488, 561, 642 nm
708 lasers; controlled by AquireSR software; image processing by SoftWorx imaging
709 software; image acquisition using an Olympus PL APO N 60x/1.42 lens with Applied
710 Precision Immersion Oil (N = 1.518)) available at the Light Microscopy Imaging Center,
711 Indiana University, Bloomington. Whenever possible, samples to be compared were
712 collected under identical settings on the same day, image files were adjusted
713 simultaneously using Adobe Photoshop CC, and figures were assembled using Adobe
714 Illustrator CC. ImageJ FIJI (https://fiji.sc/) Analyze Particles plugin was used to quantify
715 the average area of granules using 0.01µm^2 as the lower cut off of puncta size. The
716 ImageJ FIJI Plot Profile plugin was used to generate line plots.
717
718 ***Ex vivo treatments:***

719 All *ex-vivo* treatments were performed as described in Buddika et al., JCS, 2020.
720 Briefly, intestines from females aged 8-10 days on normal diet were incubated in Krebs-
721 Ringer media/KRB (Alfa Aesar, Cat. No. J67591) or KRB supplemented with 1mM
722 rapamycin (LC Laboratories, Cat. No. r-5000) for 60 min and then fixed.
723
724 ***Bleomycin feeding assay:***
725 Female flies were maintained on standard Bloomington *Drosophila* stock center media
726 for an appropriate time and then separated into two cohorts. Cohort 1 and 2 were
727 transferred to a vial with a chromatography paper soaked in either 5% sucrose in water
728 (control) or 5% sucrose and 25 µg/ml bleomycin in water, respectively. Based on
729 experiments, flies were dissected 24-to-36 hours after feeding.
730
731 ***Protein isolation and western blot analysis:***
732 Wandering L3 larvae or adult female flies were used for protein isolation. Collected
733 larvae or adult flies were lysed in I-RIPA protein lysis buffer (150mM NaCl, 50mM Tris-
734 HCl pH 7.5, 1mM EDTA, 1% Triton X-100, 1% Na Deoxycholic Acid, 1xprotease
735 inhibitor cocktail), protein extracts were resolved on a 4-20% gradient polyacrylamide
736 gel (Bio-Rad, Cat. No. 456-1093), transferred to Immobilon®-P membrane (Millipore,
737 Cat. No. IPVH00010) and probed with rat anti-TRAL (1:2000, this study), rat anti-PATR1
738 (Pradhan et al., 2012) (1:2000) or mouse anti-a-tubulin (12G10, Developmental Studies
739 Hybridoma Bank, 1:1000) antibodies. Subsequently, blots were washed extensively with
740 1xTBST (1xTBS, 0.1% Tween-20) and incubated with anti-rat or -mouse conjugated
741 HRP secondary antibodies. After extensive secondary washes with 1xTBST, blots were
742 treated with ECL-detection reagent 1 and 2 (Thermo Scientific, Cat. No. 1859701 and
743 1859698) and finally exposed to chemiluminescence films (GE Healthcare, Cat. No.
744 28906839) and developed the signal.
745
746 ***FACS isolation of progenitor cells, RNA-seq library preparation and qPCR:***
747 Gastrointestinal (GI) tracts of 100 adult female flies (per replicate) were dissected in ice-
748 cold 1xPBS. Then cells were dissociated by treating intestines with 1mg/ml elastase at
749 27°C for 1 hour with agitation. Subsequently, ~30,000-50,000 GFP^{+} intestinal progenitor

750 cells were sorted using a BD FACSAria™ II flow cytometer equipped with a 100µm
751 nozzle at the IUB Flow Cytometry Core Facility. Total RNA was prepared using the
752 TRIzol® LS reagent (Ambion). The rRNA-depleted libraries were prepared using the
753 Ovation® SoLo RNA-seq system (Part No. 0502 including Parts 0407 and S02240)
754 following manufacturer's instructions. The quality and quantity of final libraries were
755 assessed using Agilent 2200 TapeStation and KAPA Library Quantification Kit,
756 respectively. For qPCR, resulting RNA was first treated with Turbo DNase
757 (ThermoFisher, AM2239) and gDNA-free RNA used for cDNA synthesis with
758 Superscript III (ThermoFisher, 56575). qPCR was performed using the PowerUp SYBR
759 Green Master Mix (ThermoFisher, A25742) on a StepOnePlus machine
760 (ThermoFisher). Primers for all targets detected are listed in **Table S3**. Transcript levels
761 were quantified in triplicates and normalized to *Gapdh1*. Fold enrichment was calculated
762 as the ratio of transcript in genetic manipulation versus control.
763
764 ***RNA-seq data analysis:***
765 Transcriptomic data analysis was performed as described in Buddika et al., 2020a using
766 a python based in-house pipeline (https://github.com/jkkbuddika/RNA-Seq-Data-
767 Analyzer). Briefly, the quality of raw sequencing files was assessed using FastQC
768 (Andrews, 2010) version 0.11.9, low quality reads were eliminated using Cutadapt
769 (Martin, 2011) version 2.9, and reads mapping to rRNAs were removed using TagDust2
770 (Lassmann, 2015) version 2.2. Next, the remaining reads were mapped to the Berkeley
771 *Drosophila* Genome Project (BDGP) assembly release 6.28 (Ensembl release 100)
772 reference genome using STAR genome aligner (Dobin et al., 2013) version 2.7.3a and
773 duplicated reads were removed using SAMtools (Li et al., 2009) version 1.10.
774 Subsequently, the Subread (Liao et al., 2019) version 2.0.0 function *featureCounts* was
775 used to count the number of aligned reads to the nearest overlapping feature. Finally,
776 bigWig files representing RNA-seq coverage were generated using deepTools (Ramírez
777 et al., 2016) version 3.4.2 with the settings --normalizeUsing CPM --binSize 1.
778 Differential gene expression analysis was performed with the Bioconductor package
779 DESeq2 (https://bioconductor.org/packages/release/bioc/html/DESeq2.html) (Love et
780 al., 2014) version 1.26.0. Unless otherwise noted, significantly upregulated and

781 downregulated genes were defined as FDR < 0.05; Log_2 fold change > 1 and FDR <
782 0.05; Log_2 fold change < -1, respectively and were used to identify enriched Gene
783 Ontology (GO) terms using PANTHER overrepresentation analysis on GO Consortium
784 (http://geneontology.org/). A selected significantly enriched GO categories were plotted.
785 All data visualization steps were performed using custom scripts written using R.
786
787 ***Statistical analysis:***
788 GraphPad Prism, Version 7.0 was used for all statistical analyses. First, the normality of
789 datasets was tested using D'Agostino-Pearson test. For comparisons involved in two
790 datasets, if datasets follow [1] a parametric distribution, an Unpaired t-test or [2] a non-
791 parametric distribution, a Mann-Whitney test was performed. Three or more datasets
792 following a parametric distribution were analyzed using an ordinary one-way ANOVA
793 test. Multiple comparisons of three or more datasets following a non-parametric
794 distribution were analyzed using Kruskal-Wallis test. Unless otherwise noted,
795 significance is indicated as follows: n.s., not significant; *p < 0.05; **p < 0.01; ***p <
796 0.001; ****p < 0.0001.
797
798 ***Data availability:***
799 The control and *Patr-1* RNAi RNA-seq datasets from this study have been submitted to the
800 NCBI Gene Expression Omnibus under accession number XXXXXX.
801

Supplemental Information and Legends

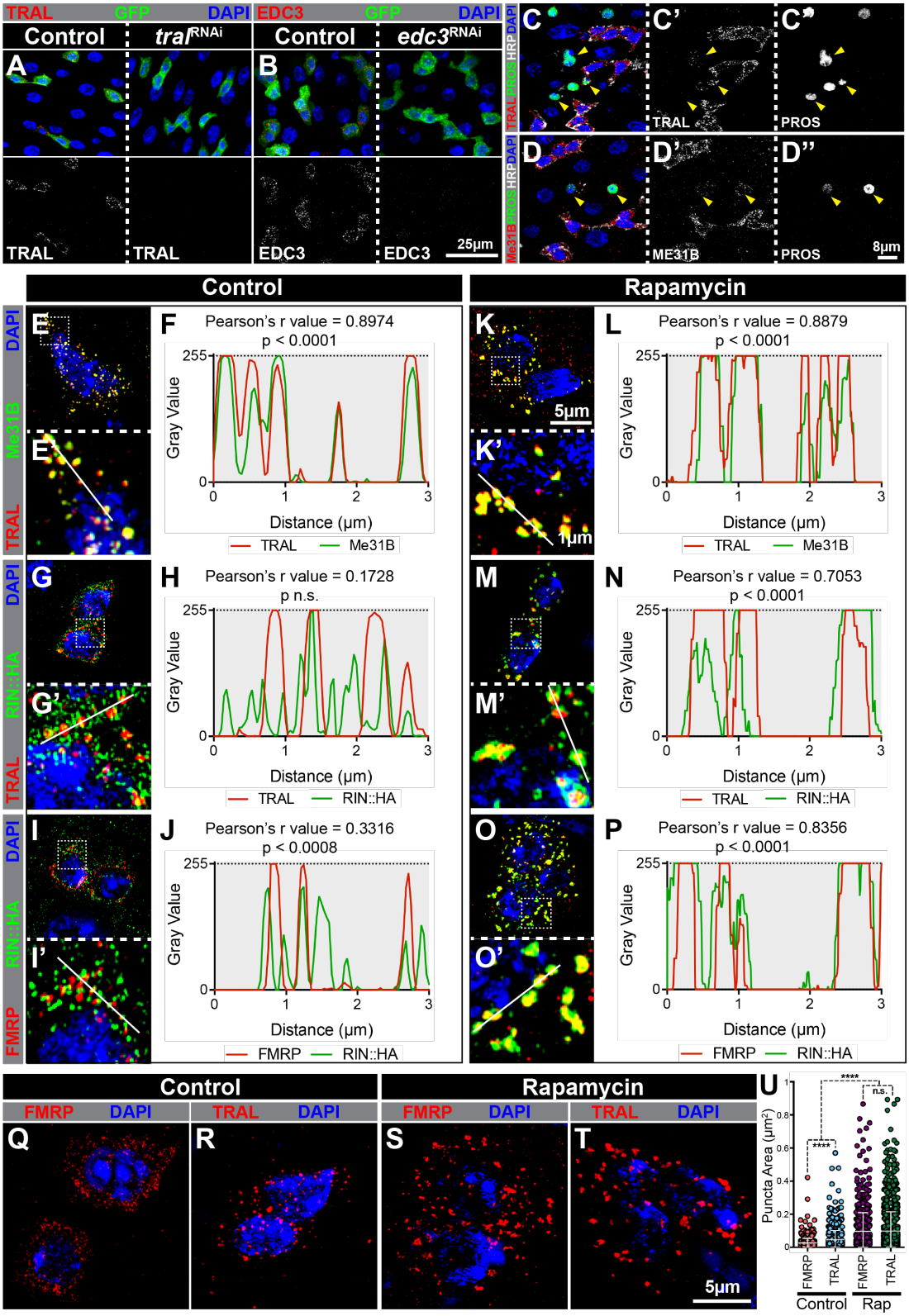

805 **Figure S1:** Comparative analysis of P-body and stress granule component expression.
806 (A-B) Progenitor cells from (A) *esg*^{TS} (control, left), *esg*^{TS} / *tral* RNAi (right) or (B) *esg*^{TS}
807 (control, left), *esg*^{TS} / *edc3* RNAi (right) intestines stained for (A) TRAL (red) or (B) EDC3
808 (red). Note that *tral* or *edc3* mutant GFP+ intestinal progenitors have no detectable
809 TRAL or EDC3 staining, respectively. (C-D) Confocal micrographs of intestinal sections
810 stained for (C) TRAL (red) or (D) Me31B (red), (C-D) PROS (green), (C-D) HRP (white)
811 and (C-D) DAPI. While TRAL and Me31B granules are readily observed in all HRP+
812 intestinal progenitors, only some Prospero+ EEs have detectable TRAL or Me31B
813 expression. (E, G, I, K, M, O) Super-resolution micrographs of progenitor cells treated
814 with either (E, G, I) KRB or (K, M, O) 1mM rapamycin in KRB and stained for (E, K)
815 TRAL (red), Me31B (green) or (G, M) TRAL (red), RIN::HA (green) or (I, O) FMRP
816 (red), RIN::HA (green) and DAPI (blue in E, G, I, K, M, O). E', G', I', K', M', and O' show
817 a magnified view of the region marked with white dotted outline in E, G, I, K, M, and O
818 respectively. (F, H, J, L, N, P) Line plots of fluorescent intensity profiles of (F, L) TRAL
819 (red), Me31B (green) or (H, N) TRAL (red), RIN::HA (green) or (J, P) FMRP (red),
820 RIN::HA (green). The plot shows the pixel-by-pixel gray value of each channel along
821 white lines in E', G', I', K', M' or O'. Computed Pearson's r value and the statistical
822 significance of the correlation are given above each plot. Note that Me31B and TRAL
823 are P-body proteins while FMRP and RIN::HA are stress granule proteins. (Q-T) Super-
824 resolution micrographs of progenitor cells treated with either (Q-R) KRB (control) or (S-
825 T) 1mM rapamycin in KRB, and stained for (Q, S) FMRP (red) or (R, T) TRAL (red) and
826 (Q-R) DAPI (blue). (U) Scatter dot plots of FMRP or TRAL puncta area in progenitor
827 cells treated with control (n=629 or 657) or 1mM rapamycin (n=804 or 1215) in KRB.
828 Error bars on plots show mean±s.d. and asterisks denote statistical significance from
829 Kruskal-Wallis test (I) $^{**}p < 0.01$; $^{****}p < 0.0001$; n.s., not significant.
830

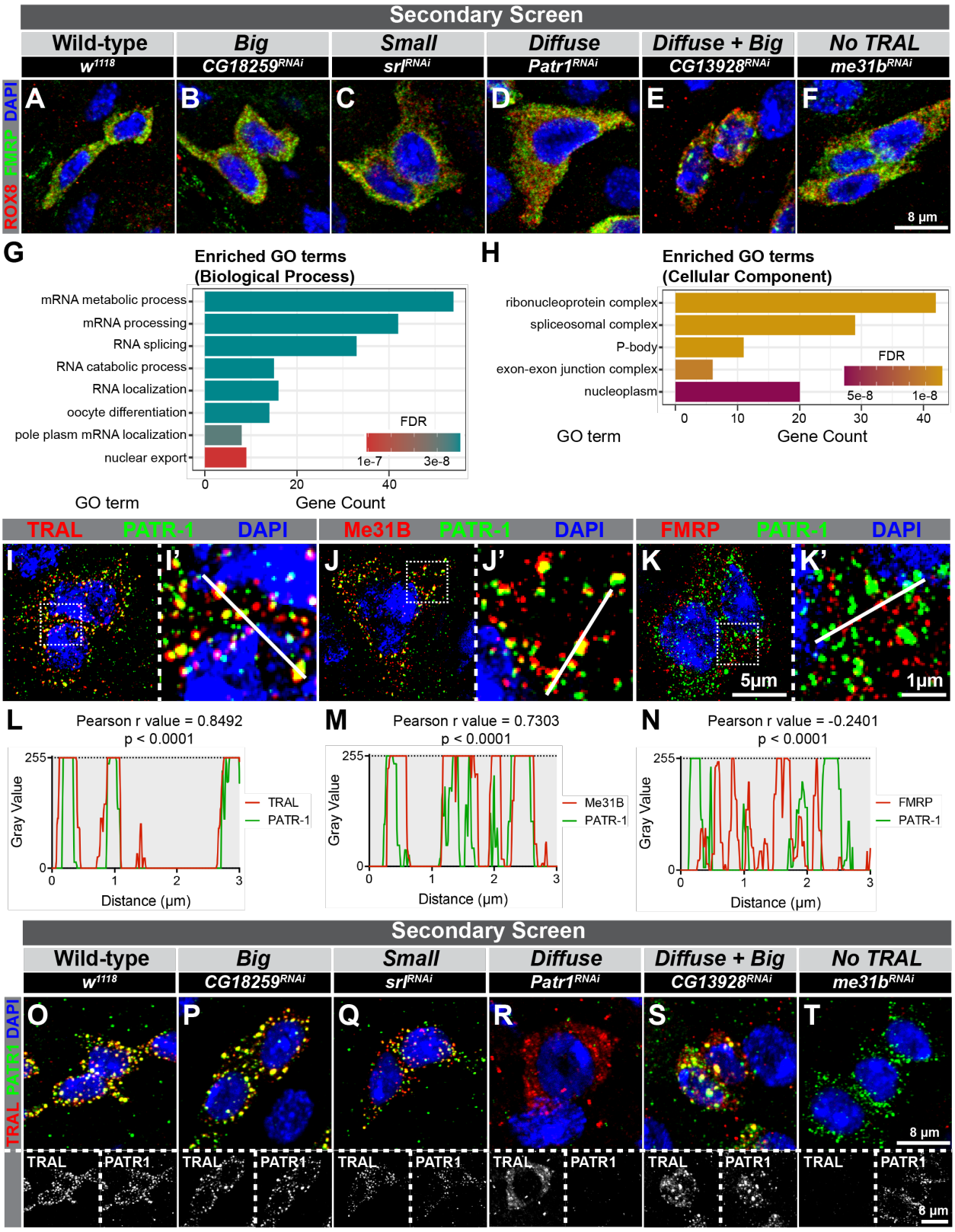

Figure S2: A targeted genetic screen identifies genes affecting P-body morphology including the P-body component, PATR-1. (A-F) Confocal micrographs of intestinal

834 progenitors from (A) *esg*^{TS}, (B) *esg*^{TS} / *CG18259* RNAi, (C) *esg*^{TS} / *srl* RNAi, (D) *esg*^{TS} /
835 *Patr-1* RNAi, (E) *esg*^{TS} / *CG13928* RNAi or (F) *esg*^{TS} / *me31b* RNAi posterior midguts
836 and stained for ROX8 (red), FMRP (green) and DAPI (blue). (G-H) Bar plots visualizing
837 significantly enriched (G) biological process or (H) cellular component Gene Ontology
838 (GO) terms (FDR < 0.05) for positive genes. The y-axis represents significantly enriched
839 GO term and the x-axis represent gene count for each GO term. Color of each bar
840 represent the FDR. (I-K) Super-resolution micrographs of intestinal progenitors stained
841 for (I-I') TRAL (red), PATR-1 (green) or (J-J') Me31B (red), PATR-1 (green) or (K-K')
842 FMRP (red), PATR-1 (green) and DAPI (blue in I-K and I'-K'). (L-N) Line plots showing
843 fluorescent intensity profiles of (L) TRAL (red) or (M) Me31B (red) or (N) FMRP (red)
844 and PATR-1 (green). The plot shows the normalized pixel-by-pixel gray value of each
845 channel along white lines shown on I'-K'. Computed Pearson's r values and the
846 statistical significance of the correlation are given above each plot. (O-T) Confocal
847 micrographs of intestinal progenitors from (O) *esg*^{TS}, (P) *esg*^{TS} / *CG18259* RNAi, (Q)
848 *esg*^{TS} / *srl* RNAi, (R) *esg*^{TS} / *Patr-1* RNAi, (S) *esg*^{TS} / *CG13928* RNAi or (T) *esg*^{TS} /
849 *me31b* RNAi posterior midguts and stained for TRAL (red), PATR-1 (green) and DAPI
850 (blue). Gray-scale images of TRAL and PATR-1 in panels are shown below the
851 respective panel.

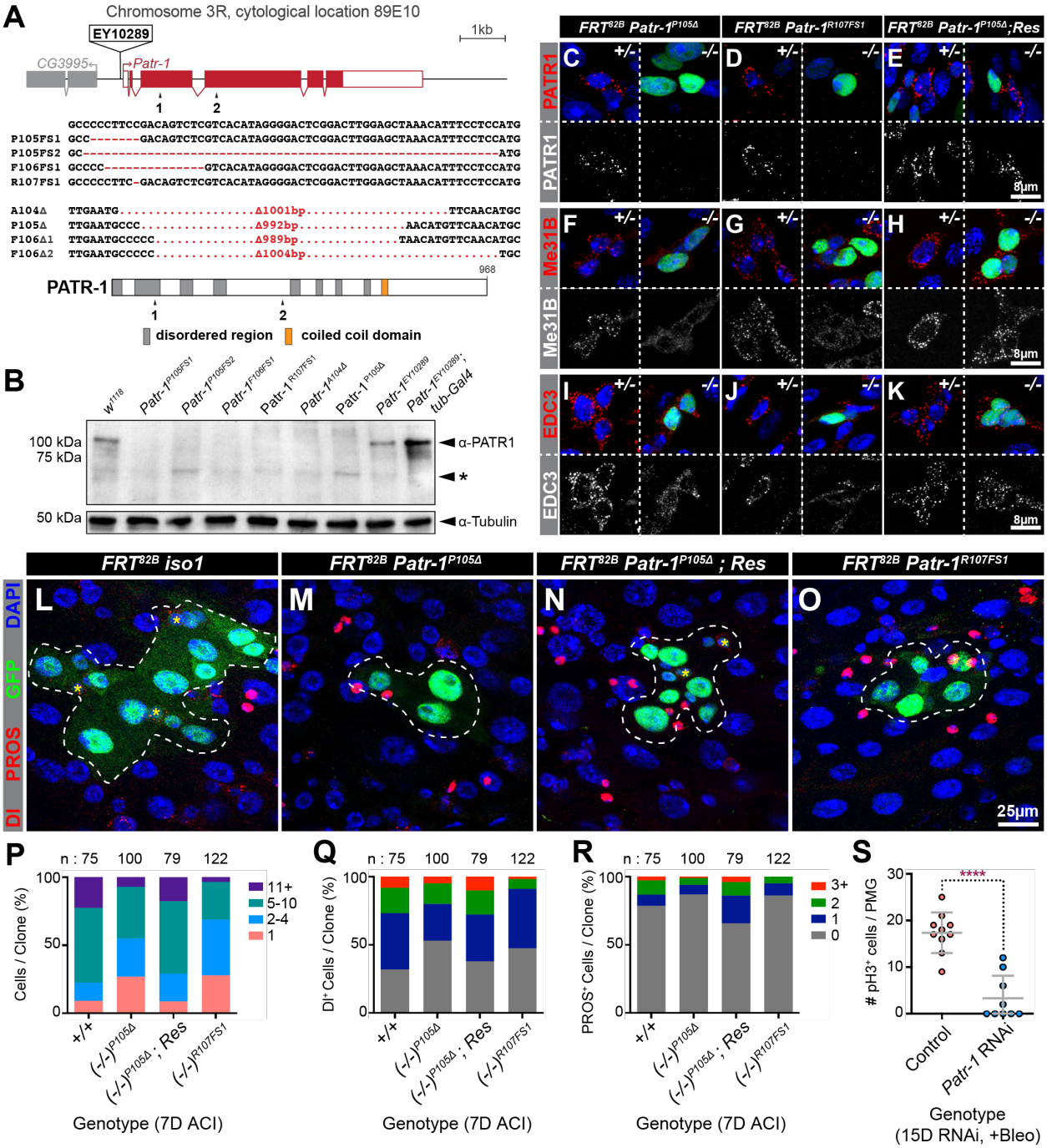

Figure S3: Loss of *Patr-1* blocks P-body formation, reduces the number of ISCs and total number of cells per clone. (A) Schematics of the *Patr-1* locus and PATR-1 protein showing the locations of the two gRNAs (arrowheads) used to generate new alleles as well as the nucleotide changes associated with these alleles. (B) Western blot of w^{1118} (control), *Patr-1* mutant, and $Patr1^{EY10289}$ / *tub-GAL4* larval extracts probed with anti-PATR-1 (top panel) or Tubulin (bottom panel) antibodies. A prominent background band

859 detected by the PATR-1 antibody is labeled (*). (C-K) MARCM-labeled homozygous
860 mutant (right, -/-) and neighboring unlabeled heterozygous (left, +/-) *Patr-1*$^{P105\Delta}$ (C, F, I),
861 *Patr-1*^{R107FS1} (D, G, J), or rescued *Patr-1*$^{P105\Delta}$ (E, H, K) progenitor cells stained for GFP
862 (green), DAPI (blue) and either PATR-1 (red in C-E), Me31B (red in F-H) or EDC3 (red
863 in I-K). (L-O) Representative confocal images of *tub-Gal4, UAS-GFP*-labeled (L) control,
864 (M) *Patr-1*$^{P105\Delta}$, (N) rescued *Patr-1*$^{P105\Delta}$, or (O) *Patr-1*^{R107FS1} homozygous clones stained
865 for Dl (red), PROS (red), GFP (green) and DAPI (blue). The size of the clone is marked
866 by the white dotted line and ISCs in clones are denoted by the yellow asterisks (*). (P-
867 R) Binned bar plots showing the quantification of (P) total cell, (Q) Dl+ ISC or (R)
868 PROS+ EE cell numbers in *tub-Gal4, UAS-GFP*-labeled control, *Patr-1*$^{P105\Delta}$, rescued
869 *Patr-1*$^{P105\Delta}$, or *Patr-1*^{R107FS1} homozygous clones analyzed 7 days after clone induction
870 (ACI). Note that n indicates the total number of clones analyzed for each genotype. (S)
871 Dot-plot showing the total number of pH3+ mitotic cells per posterior midgut of *esg*^{TS}
872 (n=10) or *esg*^{TS} / *Patr-1* RNAi (n=9) flies fed with bleomycin for 24 hours. Rescued (Res)
873 strains harbor the *Patr-1* rescuing transgene, *P21M20*.

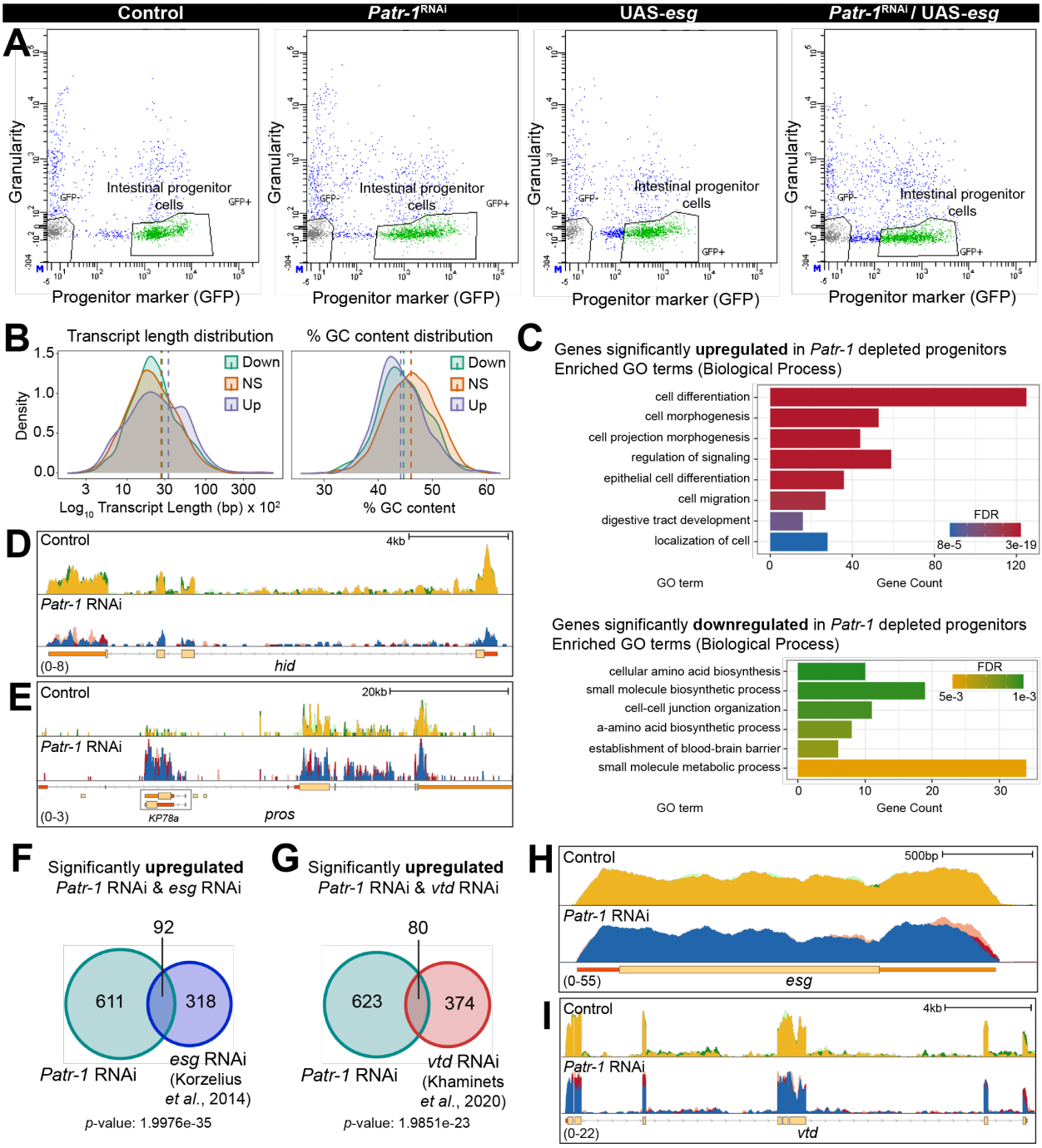

Figure S4: Gene expression changes associated with *Patr-1* RNAi. (A) FACS profiles of *esg*^{TS}, *esg*^{TS} / *Patr-1 RNAi*, *esg*^{TS} / *UAS-esg*, and *esg*^{TS} / *Patr-1 RNAi* / *UAS-esg* intestines. (B) Density plot showing the $\log_{10}$ transcript length distribution or % GC content of significantly upregulated (Up, purple), downregulated (Down, green) or unchanged (NS, orange) genes. (C) Bar plot showing a selected set of significantly enriched Gene Ontology (GO) terms for genes that are significantly upregulated or

881 downregulated in *Patr-1* RNAi compared to control. (D-E) Genome browser tracks of
882 CPM-normalized control and *Patr-1* RNAi at the (D) *hid* and (G) *pros* loci. (F, G) Venn
883 diagrams of overlap between significantly upregulated genes in *Patr-1* RNAi and (F) *esg*
884 RNAi (Korzelius et al., 2014), or (G) *vtd* RNAi (Khaminets et al., 2020). Note that
885 datasets from Korzelius et al., 2014 and Khaminets et al., 2020 were reanalyzed with
886 *Patr-1* RNAi using the in-house analysis pipeline. (H-I) Genome browser tracks of CPM-
887 normalized control and *Patr-1* RNAi at the (H) *esg* and (I) *vtd* loci. Note the three
888 replicates of the control (yellow, light green and dark green) and the three replicates of
889 the *Patr-1* RNAi (blue, pink and red) on D-E and H-I, have been overlayed for simplicity.

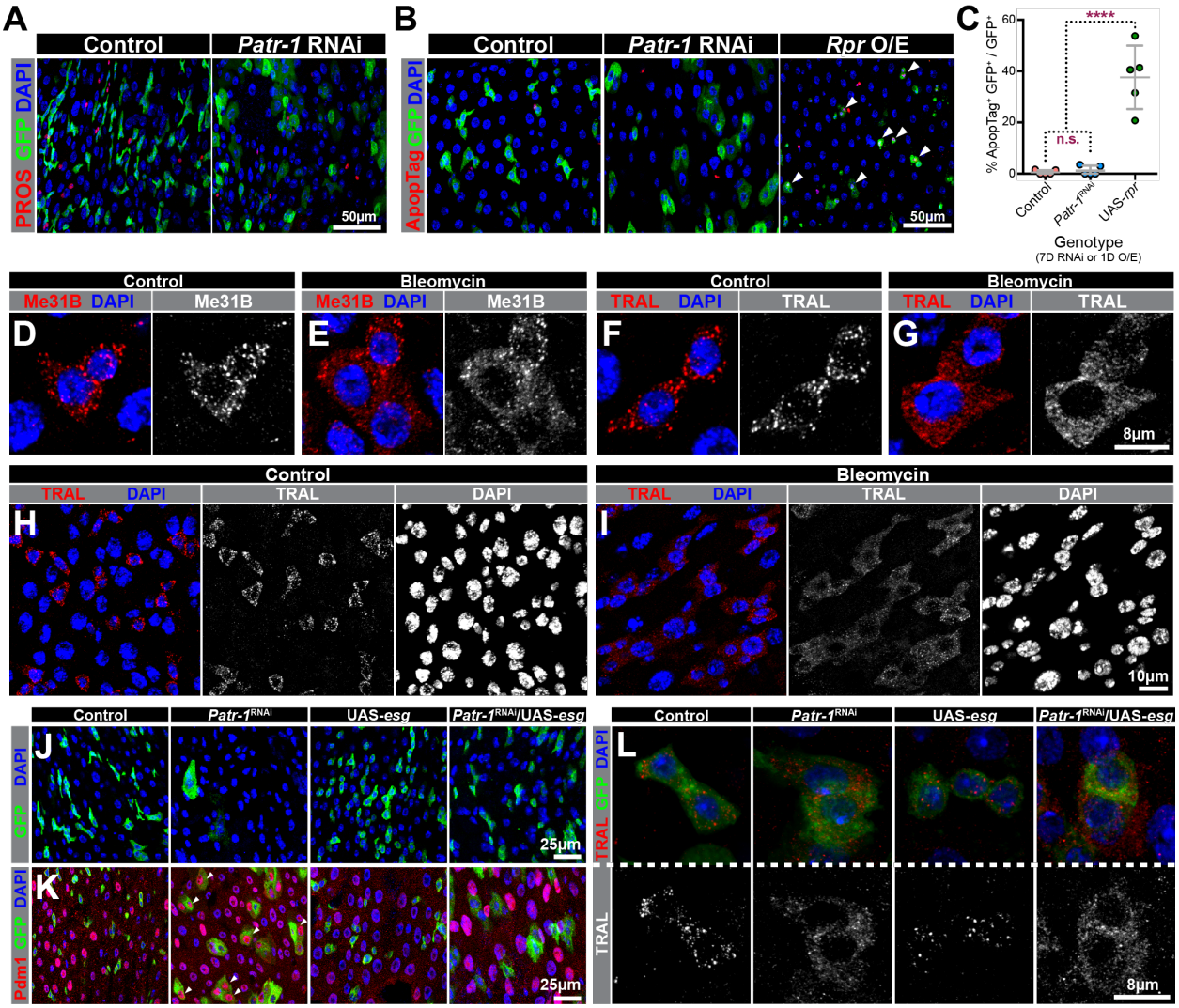

Figure S5: *Patr-1* RNAi does not lead to an increase in the number of EEs or the amount of cell death. (A-B) Confocal micrographs of intestinal sections from (A) esg^{TS} and esg^{TS} / *Patr-1* RNAi or (B) esg^{TS}, esg^{TS} / *Patr-1* RNAi and esg^{TS} / UAS-*rpr* and stained for (A) PROS (red) or (B) ApopTag (red) and GFP (green) and DAPI (blue). White arrowheads on B show ApopTag^{+} GFP^{+} cells in the field. (C) Plot of normalized ApopTag^{+} progenitor cells in esg^{TS} (n=5), esg^{TS} / *Patr-1* RNAi (n=5), and esg^{TS} / *UAS-rpr* (n=5) midguts after 7 days of RNAi or 1 day of *rpr* overexpression at 29°C. (D-I) Fluorescent micrographs of intestinal sections from w1118 flies fed with (D, F, H) 5% sucrose in water (control) or (E, G, I) 5% sucrose and 25 µg/ml bleomycin in water (bleomycin) and stained for Me31B (red in D-E) or TRAL (red in F-I) and DAPI (blue in D-I). Note that H-I show broad view images of intestines after each feeding. (J-K)

902 Sections from *esg*^{TS}, *esg*^{TS} / *Patr-1 RNAi*, *esg*^{TS} / *UAS-esg*, or *esg*^{TS} / *Patr-1 RNAi* /
903 *UAS-esg* intestines stained for Pdm1 (red, only in K), GFP (green, J-K) and DAPI (blue,
904 J-K). (L) Confocal micrographs of intestinal progenitors from *esg*^{TS}, *esg*^{TS} / *Patr-1* RNAi,
905 *esg*^{TS} / *UAS-esg*, or *esg*^{TS} / *Patr-1 RNAi / UAS-esg* posterior midguts stained for TRAL
906 (red), GFP (green) and DAPI (blue). Error bars on plots show mean±s.d. and asterisks
907 denote statistical significance from Ordinary one-way ANOVA with Turkey's multiple
908 comparison test (H). ****$p < 0.0001$, n.s. = not significant.
909
910
911

912 **References**

913 Amcheslavsky, A., Jiang, J., and Ip, Y.T. (2009). Tissue damage-induced intestinal stem
914 cell division in Drosophila. Cell Stem Cell *4*, 49–61.
915 Anderson, P., and Kedersha, N. (2006). RNA granules. J. Cell Biol. *172*, 803–808.
916 Anderson, P., and Kedersha, N. (2009). Stress granules. Curr. Biol. *19*, R397-8.
917 Andrews, S. (2010). FastQC: A quality control tool for high throughput sequence data.
918 Antonello, Z.A., Reiff, T., Ballesta-Illan, E., and Dominguez, M. (2015). Robust intestinal
919 homeostasis relies on cellular plasticity in enteroblasts mediated by miR-8–Escargot
920 switch. EMBO J. *34*, 2025–2041.
921 Ayache, J., Bénard, M., Ernoult-Lange, M., Minshall, N., Standart, N., Kress, M., and
922 Weil, D. (2015). P-body assembly requires DDX6 repression complexes rather than
923 decay or Ataxin2/2L complexes. Mol. Biol. Cell *26*, 2579–2595.
924 Barbee, S.A., Estes, P.S., Cziko, A.-M., Hillebrand, J., Luedeman, R.A., Coller, J.M.,
925 Johnson, N., Howlett, I.C., Geng, C., Ueda, R., et al. (2006). Staufen- and FMRP-
926 containing neuronal RNPs are structurally and functionally related to somatic P bodies.
927 Neuron *52*, 997–1009.
928 Bhattacharyya, S.N., Habermacher, R., Martine, U., Closs, E.I., and Filipowicz, W.
929 (2006). Relief of microRNA-Mediated Translational Repression in Human Cells
930 Subjected to Stress. Cell *125*, 1111–1124.
931 Brengues, M., Teixeira, D., and Parker, R. (2005). Decapping and Decay of Messenger
932 RNA Occur in Cytoplasmic Processing Bodies. Science (80-.). *300*, 805–808.
933 Buchan, J.R., and Parker, R. (2009). Eukaryotic Stress Granules: The Ins and Outs of
934 Translation. Mol. Cell *36*, 932–941.
935 Buddika, K., Ariyapala, I.S., Hazuga, M.A., Riffert, D., and Sokol, N.S. (2020a).
936 Canonical nucleators are dispensable for stress granule assembly in Drosophila
937 intestinal progenitors. J. Cell Sci. *133*.
938 Buddika, K., Xu, J., Ariyapala, I.S., and Sokol, N.S. (2020b). I-KCKT allows dissection-
939 free RNA profiling of adult Drosophila intestinal progenitor cells . Development *148*,
940 dev.196568.
941 Buddika, K., Xu, J., Ariyapala, I.S., and Sokol, N.S. (2020c). I-KCKT allows dissection-
942 free RNA profiling of adult Drosophila intestinal progenitor cells. BioRxiv.

943 Chan, L.Y., Mugler, C.F., Heinrich, S., Vallotton, P., and Weis, K. (2018). Non-invasive
944 measurement of mRNA decay reveals translation initiation as the major determinant of
945 mRNA stability. Elife *7*.
946 Chen, Q., and Hu, G. (2017). Post-transcriptional regulation of the pluripotent state.
947 Curr. Opin. Genet. Dev. *46*, 15–23.
948 Chen, C.-H., Luhur, A., and Sokol, N. (2015). Lin-28 promotes symmetric stem cell
949 division and drives adaptive growth in the adult Drosophila intestine. Development *142*,
950 3478–3487.
951 Coller, J., and Parker, R. (2005). General translational repression by activators of
952 mRNA decapping. Cell *122*, 875–886.
953 Courel, M., Clément, Y., Bossevain, C., Foretek, D., Cruchez, O.V., Yi, Z., Bénard, M.,
954 Benassy, M.N., Kress, M., Vindry, C., et al. (2019). Gc content shapes mRNA storage
955 and decay in human cells. Elife *8*.
956 Decker, C.J., and Parker, R. (2012). P-Bodies and Stress Granules: Possible Roles in
957 the Control of Translation and mRNA Degradation. Cold Spring Harb. Perspect. Biol. *4*,
958 a012286.
959 Dobin, A., Davis, C.A., Schlesinger, F., Drenkow, J., Zaleski, C., Jha, S., Batut, P.,
960 Chaisson, M., and Gingeras, T.R. (2013). STAR: ultrafast universal RNA-seq aligner.
961 Bioinformatics *29*, 15–21.
962 Eulalio, A., Behm-Ansmant, I., Schweizer, D., and Izaurralde, E. (2007a). P-body
963 formation is a consequence, not the cause, of RNA-mediated gene silencing. Mol. Cell.
964 Biol. *27*, 3970–3981.
965 Eulalio, A., Behm-Ansmant, I., and Izaurralde, E. (2007b). P bodies: at the crossroads
966 of post-transcriptional pathways. Nat. Rev. Mol. Cell Biol. *8*, 9–22.
967 Fan, S.-J., Marchand, V., and Ephrussi, A. (2011). Drosophila Ge-1 Promotes P Body
968 Formation and oskar mRNA Localization. PLoS One *6*, e20612.
969 Franks, T.M., and Lykke-Andersen, J. (2008). The Control of mRNA Decapping and P-
970 Body Formation. Mol. Cell *32*, 605–615.
971 Hubstenberger, A., Courel, M., Bénard, M., Souquere, S., Ernoult-Lange, M., Chouaib,
972 R., Yi, Z., Morlot, J.-B., Munier, A., Fradet, M., et al. (2017). P-Body Purification Reveals
973 the Condensation of Repressed mRNA Regulons. Mol. Cell *68*, 144-157.e5.

974 Jain, S., Wheeler, J.R., Walters, R.W., Agrawal, A., Barsic, A., and Parker, R. (2016).
975 ATPase-Modulated Stress Granules Contain a Diverse Proteome and Substructure.
976 Cell *164*, 487–498.
977 Kedersha, N., Cho, M.R., Li, W., Yacono, P.W., Chen, S., Gilks, N., Golan, D.E., and
978 Anderson, P. (2000). Dynamic Shuttling of Tia-1 Accompanies the Recruitment of
979 mRNA to Mammalian Stress Granules. J. Cell Biol. *151*, 1257–1268.
980 Kedersha, N., Stoecklin, G., Ayodele, M., Yacono, P., Lykke-Andersen, J., Fritzler, M.J.,
981 Scheuner, D., Kaufman, R.J., Golan, D.E., and Anderson, P. (2005). Stress granules
982 and processing bodies are dynamically linked sites of mRNP remodeling. J. Cell Biol.
983 *169*, 871–884.
984 Khaminets, A., Ronnen-Oron, T., Baldauf, M., Meier, E., and Jasper, H. (2020). Cohesin
985 controls intestinal stem cell identity by maintaining association of Escargot with target
986 promoters. Elife *9*.
987 Korzelius, J., Naumann, S.K., Loza-Coll, M.A., Chan, J.S., Dutta, D., Oberheim, J.,
988 Gläßer, C., Southall, T.D., Brand, A.H., Jones, D.L., et al. (2014). *Escargot* maintains
989 stemness and suppresses differentiation in *Drosophila* intestinal stem cells. EMBO J.
990 *33*, 2967–2982.
991 Lassmann, T. (2015). TagDust2: a generic method to extract reads from sequencing
992 data. BMC Bioinformatics *16*, 24.
993 Lee, T., and Luo, L. (1999). Mosaic Analysis with a Repressible Cell Marker for Studies
994 of Gene Function in Neuronal Morphogenesis. Neuron *22*, 451–461.
995 Li, H., Handsaker, B., Wysoker, A., Fennell, T., Ruan, J., Homer, N., Marth, G.,
996 Abecasis, G., Durbin, R., and 1000 Genome Project Data Processing Subgroup (2009).
997 The Sequence Alignment/Map format and SAMtools. Bioinformatics *25*, 2078–2079.
998 Li, Y., Pang, Z., Huang, H., Wang, C., Cai, T., and Xi, R. (2017). Transcription Factor
999 Antagonism Controls Enteroendocrine Cell Specification from Intestinal Stem Cells. Sci.
1000 Rep. *7*, 988.
1001 Liao, Y., Smyth, G.K., and Shi, W. (2019). The R package Rsubread is easier, faster,
1002 cheaper and better for alignment and quantification of RNA sequencing reads. Nucleic
1003 Acids Res. *47*, e47.
1004 Liu, Q., and Jin, L.H. (2017). Tissue-resident stem cell activity: a view from the adult

1005 Drosophila gastrointestinal tract. Cell Commun. Signal. *15*, 33.
1006 Love, M.I., Huber, W., and Anders, S. (2014). Moderated estimation of fold change and
1007 dispersion for RNA-seq data with DESeq2. Genome Biol. *15*, 550.
1008 Loza-Coll, M.A., Southall, T.D., Sandall, S.L., Brand, A.H., and Jones, D.L. (2014).
1009 Regulation of Drosophila intestinal stem cell maintenance and differentiation by the
1010 transcription factor Escargot. EMBO J. *33*, 2983–2996.
1011 Luhur, A., Buddika, K., Ariyapala, I.S., Chen, S., and Sokol, N.S. (2017). Opposing
1012 Post-transcriptional Control of InR by FMRP and LIN-28 Adjusts Stem Cell-Based
1013 Tissue Growth. Cell Rep. *21*, 2671–2677.
1014 Luo, Y., Na, Z., and Slavoff, S.A. (2018). P-Bodies: Composition, Properties, and
1015 Functions. Biochemistry *57*, 2424–2431.
1016 Martin, M. (2011). Cutadapt removes adapter sequences from high-throughput
1017 sequencing reads. EMBnet.Journal *17*, 10.
1018 Martínez, J.P., Pérez-Vilaró, G., Muthukumar, Y., Scheller, N., Hirsch, T., Diestel, R.,
1019 Steinmetz, H., Jansen, R., Frank, R., Sasse, F., et al. (2013). Screening of small
1020 molecules affecting mammalian P-body assembly uncovers links with diverse
1021 intracellular processes and organelle physiology. RNA Biol. *10*, 1661–1669.
1022 Micchelli, C.A., and Perrimon, N. (2006). Evidence that stem cells reside in the adult
1023 Drosophila midgut epithelium. Nature *439*, 475–479.
1024 Miller, D.E., Kahsai, L., Buddika, K., Dixon, M.J., Kim, B.Y., Calvi, B.R., Sokol, N.S.,
1025 Scott Hawley, R., and Cook, K.R. (2020). Identification and characterization of
1026 breakpoints and mutations on drosophila melanogaster balancer chromosomes. G3
1027 Genes, Genomes, Genet. *10*, 4271–4285.
1028 Mugler, C.F., Hondele, M., Heinrich, S., Sachdev, R., Vallotton, P., Koek, A.Y., Chan,
1029 L.Y., and Weis, K. (2016). ATPase activity of the DEAD-box protein Dhh1 controls
1030 processing body formation. Elife *5*.
1031 Nakamura A, Amikura R, Hanyu K, K.S. (2001). Me31B silences translation of oocyte-
1032 localizing RNAs through the formation of cytoplasmic RNP complex during Drosophila
1033 oogenesis. Development *128*, 3233–3242.
1034 Niewidok, B., Igaev, M., Pereira da Graca, A., Strassner, A., Lenzen, C., Richter, C.P.,
1035 Piehler, J., Kurre, R., and Brandt, R. (2018). Single-molecule imaging reveals dynamic

1036 biphasic partition of RNA-binding proteins in stress granules. J. Cell Biol. *217*, 1303–
1037 1318.
1038 Nissan, T., Rajyaguru, P., She, M., Song, H., and Parker, R. (2010). Decapping
1039 activators in Saccharomyces cerevisiae act by multiple mechanisms. Mol. Cell *39*, 773–
1040 783.
1041 Van Nostrand, E.L., Pratt, G.A., Shishkin, A.A., Gelboin-Burkhart, C., Fang, M.Y.,
1042 Sundararaman, B., Blue, S.M., Nguyen, T.B., Surka, C., Elkins, K., et al. (2016). Robust
1043 transcriptome-wide discovery of RNA-binding protein binding sites with enhanced CLIP
1044 (eCLIP). Nat. Methods *13*, 508–514.
1045 O'Brien, L.E., Soliman, S.S., Li, X., and Bilder, D. (2011). Altered Modes of Stem Cell
1046 Division Drive Adaptive Intestinal Growth. Cell *147*, 603–614.
1047 Ohlstein, B., and Spradling, A. (2006). The adult Drosophila posterior midgut is
1048 maintained by pluripotent stem cells. Nature *439*, 470–474.
1049 Parker, R., and Sheth, U. (2007). P Bodies and the Control of mRNA Translation and
1050 Degradation. Mol. Cell *25*, 635–646.
1051 Pilkington, G.R., and Parker, R. (2008). Pat1 contains distinct functional domains that
1052 promote P-body assembly and activation of decapping. Mol. Cell. Biol. *28*, 1298–1312.
1053 Pradhan, S.J., Nesler, K.R., Rosen, S.F., Kato, Y., Nakamura, A., Ramaswami, M., and
1054 Barbee, S.A. (2012). The conserved P body component HPat/Pat1 negatively regulates
1055 synaptic terminal growth at the larval Drosophila neuromuscular junction. J. Cell Sci.
1056 *125*, 6105–6116.
1057 Protter, D.S.W., and Parker, R. (2016). Principles and Properties of Stress Granules.
1058 Trends Cell Biol. *26*, 668–679.
1059 Ramírez, F., Ryan, D.P., Grüning, B., Bhardwaj, V., Kilpert, F., Richter, A.S., Heyne, S.,
1060 Dündar, F., and Manke, T. (2016). deepTools2: a next generation web server for deep-
1061 sequencing data analysis. Nucleic Acids Res. *44*, W160–W165.
1062 Sachdev, R., Hondele, M., Linsenmeier, M., Vallotton, P., Mugler, C.F., Arosio, P., and
1063 Weis, K. (2019). Pat1 promotes processing body assembly by enhancing the phase
1064 separation of the DEAD-box ATPase Dhh1 and RNA. Elife *8*.
1065 Scheller, N., Resa-Infante, P., de la Luna, S., Galao, R.P., Albrecht, M., Kaestner, L.,
1066 Lipp, P., Lengauer, T., Meyerhans, A., and Díez, J. (2007). Identification of PatL1, a

1067 human homolog to yeast P body component Pat1. Biochim. Biophys. Acta - Mol. Cell
1068 Res. *1773*, 1786–1792.
1069 Sheth, U., and Parker, R. (2003). Decapping and Decay of Messenger RNA Occur in
1070 Cytoplasmic Processing Bodies. Science (80-.). *300*, 805–808.
1071 Souquere, S., Mollet, S., Kress, M., Dautry, F., Pierron, G., and Weil, D. (2009).
1072 Unravelling the ultrastructure of stress granules and associated P-bodies in human
1073 cells. J. Cell Sci. *122*, 3619–3626.
1074 Standart, N., and Weil, D. (2018). P-Bodies: Cytosolic Droplets for Coordinated mRNA
1075 Storage. Trends Genet. *34*, 612–626.
1076 Di Stefano, B., Luo, E.-C., Haggerty, C., Aigner, S., Charlton, J., Brumbaugh, J., Ji, F.,
1077 Rabano Jiménez, I., Clowers, K.J., Huebner, A.J., et al. (2019). The RNA Helicase
1078 DDX6 Controls Cellular Plasticity by Modulating P-Body Homeostasis. Cell Stem Cell
1079 *25*, 622-638.e13.
1080 Stoecklin, G., Mayo, T., and Anderson, P. (2006). ARE-mRNA degradation requires the
1081 5′–3′ decay pathway. EMBO Rep. *7*, 72–77.
1082 Teixeira, D., and Parker, R. (2007). Analysis of P-Body Assembly in *Saccharomyces*
1083 *cerevisiae*. Mol. Biol. Cell *18*, 2274–2287.
1084 Teixeira, D., Sheth, U., Valencia-Sanchez, M.A., Brengues, M., and Parker, R. (2005).
1085 Processing bodies require RNA for assembly and contain nontranslating mRNAs. RNA
1086 *11*, 371–382.
1087 Tian, A., Wang, B., and Jiang, J. (2017). Injury-stimulated and self-restrained BMP
1088 signaling dynamically regulates stem cell pool size during Drosophila midgut
1089 regeneration. Proc. Natl. Acad. Sci. U. S. A. *114*, E2699–E2708.
1090 V, R., KH, S., and PK, H. (2011). The cAMP-dependent Protein Kinase Signaling
1091 Pathway Is a Key Regulator of P Body Foci Formation. Mol. Cell *43*.
1092 Wang, Y., Arribas-Layton, M., Chen, Y., Lykke-Andersen, J., and Sen, G.L. (2015).
1093 DDX6 Orchestrates Mammalian Progenitor Function through the mRNA Degradation
1094 and Translation Pathways. Mol. Cell *60*, 118–130.
1095 Wheeler, J.R., Matheny, T., Jain, S., Abrisch, R., and Parker, R. (2016). Distinct stages
1096 in stress granule assembly and disassembly. Elife *5*.
1097 Youn, J.-Y., Dyakov, B.J.A., Zhang, J., Knight, J.D.R., Vernon, R.M., Forman-Kay, J.D.,

1098 and Gingras, A.-C. (2019). Properties of Stress Granule and P-Body Proteomes. Mol.
1099 Cell *76*, 286–294.
1100 Zeng, X., Chauhan, C., and Hou, S.X. (2010). Characterization of midgut stem cell- and
1101 enteroblast-specific Gal4 lines in drosophila. Genesis *48*, 607–611.
1102